Agricultural Water Management 308 (2025) 109254

Contents lists available at ScienceDirect

Agricultural Water Management

journal homepage: www.elsevier.com/locate/agwat

Surface water and flood-based agricultural systems: Mapping and modelling long-term variability in the Senegal river floodplain

Andrew Ogilvie [a,b,*], Cheickh Sadibou Fall [b], Ansoumana Bodian [c], Didier Martin [a], Laurent Bruckmann [d,e], Djiby Dia [b], Issa Leye [a], Papa Malick Ndiaye [a,c], Donissongou Dimitri Soro [f], Jean Homian Danumah [f,g], Jean-Claude Bader [a], Jean-Christophe Poussin [a]

[a] *G-EAU, AgroParisTech, BRGM, Cirad, INRAE, Institut Agro, IRD, Univ Montpellier, Montpellier, France*
[b] *ISRA, BAME, Dakar, Senegal*
[c] *Laboratoire Leïdi "Dynamics of Territories and Development", Université Gaston Berger (UGB), Saint-Louis, Senegal*
[d] *Department of Civil and Water Engineering, Université Laval, Quebec, Canada*
[e] *CentrEau, Water Research Center, Quebec, Canada*
[f] *UFR Sciences de la Terre et des Ressources Minières (STRM), Université Félix Houphouët Boigny, Abidjan, Côte d'Ivoire*
[g] *CURAT, Université Félix Houphouët Boigny, Abidjan, Côte d'Ivoire*

A R T I C L E I N F O

Handling Editor - J.E. Fernández

Keywords:
Surface water
Remote sensing
West Africa
Long-term monitoring
Flood-based agricultural systems

A B S T R A C T

In the alluvial plains of large rivers, annual flooding is essential for numerous ecosystem services, including flood-based agriculture, biodiversity and groundwater recharge. Remote sensing provides increased opportunities to monitor surface water dynamics across large floodplains that are currently poorly captured by local hydrological monitoring and modelling due to data scarcity and the flat, heterogeneous topography. Combining the advances in earth observations with hydrological modelling and extensive *in situ* fieldwork, this research seeks to improve our understanding of surface water dynamics and associated agricultural practices in the Senegal river floodplain. 2813 mosaics from Landsat, MODIS and Sentinel-2 earth observations are created to map and monitor surface water variations using a site specific MNDWI classification adapted to complex, wetland environments. Validated against ground truth data, the approach is upscaled using cloud computing across this 2250 km^2 floodplain over 1999–2022. Statistical regression models are then developed to estimate flooded and cultivated areas based on upstream flow values since 1950 and analyse trends and exceedance probabilities over time. Results reveal extreme interannual variations in peak flooded areas, ranging from 30,000 ha and 720,000 ha between 1950 and 2022, while annual water modules fluctuate between 210 and 1460 m^3/s. After 1994, flooded areas show partial recovery, with 95th percentile reaching 89,000 ha during 1994–2022 compared to 37,000 ha in 1972–1993. Flood-based agricultural practices cover between 13,000 ha and 133,000 ha over the same period, highlighting the pronounced variability faced by local rural communities. Occurrence maps and predictive models for annual flooded and cultivated areas based on upstream flows can support early warning tools, helping to prepare for extreme floods and droughts. These outputs are crucial to assess the impact of future climatic and anthropic changes in the region, including planned dams, on the amplitude of annual floods and their associated environmental benefits.

1. Introduction

In the alluvial plains of large rivers, annual flooding provides numerous ecosystem services related to water and food supply, regulation, biodiversity as well as important cultural and immaterial functions. In Africa, more than 25 million hectares of alluvial floodplains are used for flood-based agricultural systems (FBAS), primarily for family and subsistence farming (Kool et al., 2018; Zenebe et al., 2022; Ayyad et al., 2022). However, these practices are conditioned by the amplitude of the annual flood, making them vulnerable to both regional climatic and anthropic changes. In semi-arid areas, hydrological regimes are particularly affected by extreme climatic variability, land use changes, and upstream interventions such as dam construction and agricultural withdrawals. The development of large dams in Asia (Hecht et al., 2019), in West Africa (Seidou et al., 2021; Tilmant et al., 2020) to meet

* Corresponding author at: G-EAU, AgroParisTech, BRGM, Cirad, INRAE, Institut Agro, IRD, Univ Montpellier, Montpellier, France.
E-mail address: andrew.ogilvie@ird.fr (A. Ogilvie).

https://doi.org/10.1016/j.agwat.2024.109254
Received 12 March 2024; Received in revised form 7 November 2024; Accepted 16 December 2024
Available online 2 January 2025

growing demands for hydropower and irrigation for example introduce major hydrological changes, reducing the amplitude of these beneficial floods. Understanding these changes and evaluating the trade-offs for the Water-energy-food-ecosystems (WEFE) nexus (Hellegers et al., 2008; Teutschbein et al., 2023; Cristiano et al., 2021) requires detailed understanding of the hydrological dynamics of these floodplains. The scale and flat topography of these floodplains lead to considerable uncertainties in the hydrological modelling of lateral overflows, despite improvements in digital elevation models (Archer et al., 2018; Hawker et al., 2018). These difficulties are exacerbated by the decline in hydrometric networks in Africa (Hannah et al., 2011; Tarpanelli et al., 2023) as well as the difficulties to understand and represent the trajectories of water resources and human activities (land use, dam management, withdrawals, etc.) and their mutual interactions.

The rising availability of earth observations (EO) with increasing spatial, temporal and spectral resolutions has led to increased opportunities to monitor and characterise temporal and spatial variations of surface water areas across large areas. Numerous works have shown the potential of EO to monitor large surface water bodies, whilst also highlighting the specific difficulties in mapping and monitoring floods in mixed water environments such as wetlands (Mahdianpari et al., 2018; Mahdavi et al., 2018). Global datasets have notably been developed and used for large scale mapping of surface waters. These include the Global Lakes and Wetlands Database (GLWD) by Lehner et al. (2011), the Global Land Cover Facility surface water dataset by Feng et al. (2015) and the Global 3sec/1 s Water Body Map (G3WBM/G1WBM) by Yamazaki et al. (2015). These products were developed using multi-temporal and multi-source imagery to distinguish land, permanent water bodies and temporally flooded areas up to 30 m resolution. Accordingly, they provide a static map of water bodies rather than monthly or annual variations. Global Surface Water (GSW) datasets by Pekel et al. (2016) provide monthly imagery based on Landsat images over 1982–2021 at 30 m resolution however their reduced repetitivity (1 image per month) limits their suitability in monitoring fine variations in small or fragmented water bodies such as wetlands (Yamazaki and Trigg, 2016). Previous works also highlighted their limitations in mixed environments such as wetlands and floodplains where shallow waters, and flooded vegetation (and vegetated water) are often undetected due to the mixed reflectance of water, vegetation and soil (Ogilvie et al., 2018, 2020a; Herndon et al., 2020; Hardy et al., 2019). Context specific classification and monitoring approaches need to be developed and optimised in multiple settings and combining multi-source imagery is essential to capture short term dynamics and long term changes (Heimhuber et al., 2018; Ogilvie et al., 2020a). The advent of cloud computing environments notably allows for combining the respective advantages of a catalogue of EO sensors (Claverie et al., 2018) in terms of spatial resolution (up to 10 m with Sentinel-2), temporal repetitivity (daily with MODIS), and depth of observations (since 1972 with Landsat) or observation mode (passive and active sensors) (Amani et al., 2019; Nguyen et al., 2020).

In the mid-Senegal River valley, in floodplains and along riverbanks, the annual flood waters have traditionally been exploited for flood-recession crops, fishing, grazing, fibre and timber. An essential habitat for birds and other wildlife, this floodplain contains seven wetland sites of international importance listed under the Ramsar convention, including the Parc National du Djoudj in Senegal and the Parc National du Diawling in Mauritania. The droughts of the 1970s and 1980s encouraged the development of irrigation, but to this day it still only concerns a small percentage of farmland, with yields and financial results often falling short of initial expectations, and crop residues without good fodder value. Flood recession crops, in basins and on riverbanks, are still grown whenever the floodwaters are high enough, on several tens of thousands of hectares and are necessary to feed the population (and their herds) who have no access to irrigated areas (Bruckmann, 2018; Poussin et al., 2020; Sall et al., 2020b). Dam operation at Manantali on the Senegal river since 1987 to support irrigation and the development of hydroelectricity begun to modify the hydrological regimes, reducing the amplitude of floods. The downstream Diama dam completed in 1986 also raised water levels in the floodplain and two run-of-river hydroelectric plants have been commissioned in Felou (2013) and Gouina (2022) as part of the transboundary river basin development strategy (Fig. 1). Several new dams, including Gourbassi, Boureya, Balassa and Koukoutamba, are planned by the river basin agency and set to introduce major hydrological changes (BRLi et al., 2021; Raso et al., 2020). Understanding the evolution of the flooded areas is therefore essential, in order to define suitable water management and allocation strategies to optimise their operation and minimise their impacts on wetlands, as well as on flood-based agriculture in the region.

Previous research focussing on the Senegal river floodplain explored hydrological regimes and their variations following the construction of the Manantali dam (Bader, 1997; Bader et al., 2003; Sambou et al., 2019; Raso et al., 2020) as well as propagation of flows between the river bed and lateral overflows in the floodplain Ogilvie et al. (2020b), Bader et al. (2017). In particular, research led to defining objective flood hydrographs to maintain objectives of flooded areas and potential flood-recession crop areas in the floodplain. Inundation patterns were explored using eight SPOT images from the 1990s to derive a correlation between river flow and water surface areas (Lamagat and Bader, 2004). These results underpin predictive tools and water allocation models that continue to guide stakeholders in defining reservoir operation rules and assessing the impacts of future river basin development and management scenarios (SCP et al., 2009; Bader, 2015; BRLi et al., 2021). Updating and improving the scientific basis of these tools is essential to account for changes in the hydrological regime over the past three decades. Leveraging advances in earth observation science is crucial to shed light on the scale and importance of flood-based agricultural systems, which are often overlooked in favour of hydroelectric and irrigation concerns. Since the Manantali hydroelectric plant became operational in 2004, no releases have been made to support the annual floods and FBAS (Bruckmann et al., 2022). Recently, Bruckmann et al. (2022) investigated recent hydrological variations and looked at flood patterns on a single MODIS image per year at 500 m resolution on the floodplain between Dagana-Matam. In parallel, Ogilvie et al. (2020a) looked at combining multi-sensor satellite imagery to monitor flood dynamics on a subset of the floodplain around Podor, demonstrating the value of a context-specific approach at 20 m resolution adapted to the particularities of these heterogeneous environments. This research builds on earlier work and aims to provide a detailed up-to-date understanding of the scale and dynamics of flooded areas and flood recession cropping in the Senegal River floodplain. Specifically, our works seek to first provide the most comprehensive assessment of the interannual variability of inundated areas across this expansive floodplain by harnessing and comparing the effectiveness of available optical EO imagery. Secondly, regressive models are developed to estimate flooded areas based on upstream hydrological data, extrapolating trends back to 1950. Thirdly, flood mapping results are combined with field observations and data on FBAS to identify potential areas for FBAS and estimate cropped areas since 1950 across the whole floodplain.

2. Data and methods

2.1. The Senegal River and its floodplain

The Senegal River is a large transboundary basin spread over 337,000 km^2 across four countries: Guinea, Mali, Mauritania and Senegal. Downstream of Bakel, the Senegal River flows into a vast floodplain of 10–20 km wide, over the last 790 km of its rivercourse. Topography is very flat, with average decline in the rivercourse of 1–3 cm per km (Bader, 2015). Bakel corresponds to the beginning of the floodplain and is situated downstream of all the major tributaries of the Senegal River: the Falémé, Bafing and Bakoye. West of Dagana, the river flow is heavily influenced by the dykes and embankments built

Fig. 1. Location of the Senegal river basin, its floodplain and major dams. Background imagery composited from Bing satellite imagery and Verdin (2017) topography data.

during the 20th century to prevent overflow, the greater influence of the Diama dam and the numerous large irrigated perimeters notably around Richard Toll.

The Senegal floodplain situated between the towns of Dagana and Bakel was studied here (Fig. 1). These boundaries are based upon those used in previous studies (Lamagat and Bader, 2004; Bruckmann et al., 2022) but seek to include the full expanse of the floodplain, covering a total of 1,100,000 ha. The region of interest (ROI) extends further south than the area studied in the POGR (Programme d'Optimisation de la Gestion des Réservoirs) by Lamagat (2001) which focussed on the Matam-Dagana section. This choice was partly due to the spatial coverage of the satellite imagery they obtained at the time and Lamagat (2001) recognise that flooded areas upstream of Matam (between Matam and Bakel) are estimated to represent 19% of the total flooded area between Matam and Dagana. Sentinel-2 imagery confirmed that FBAS are observed in areas upstream of Matam, such as the floodplain west of Maghama as illustrated in the Sentinel-2 image from February 2020. For the same reasons, wetlands east of Kaedi were included in the ROI.

2.2. Earth observation mapping and monitoring of flooded areas

Images from MODIS Terra, Landsat 5–7 and 8, and Sentinel-2 satellites were used to combine their respective strengths in terms of spatial resolution, temporal resolution and temporal coverage. The complete archive of images per year was used rather than a single image close to the flood peak, to ensure the flood peak is accurately captured. In the Senegal floodplain, the timing of peak waters varies according to the amplitude of the flood and the location along the floodplain. The flood is effectively slowed by the friction of spreading across the floodplain, meaning that a large flood will progress slower than a minor flood (Bader et al., 2017). The peak in Podor occurs in mid-October during a large flood, and in early September in low flood years. At Bakel 500 kilometres upstream, the flood peak occurs in early September and late August respectively. The Google Earth Engine (GEE) Cloud computing platform (Gorelick et al., 2017) is used here to reduce downloading and geoprocessing times considerably, essential when multiplying image sources, tiles and time periods. A total of 2813 mosaics for MODIS, Landsat, and Sentinel-2 over 1984–2022 were created and processed in GEE.

2.2.1. Earth observation data

Imagery from the MODIS sensor aboard the Terra satellite were accessed via Google Earth Engine (asset MODIS/006/MOD09A1). With its wide swath, this medium spatial resolution sensor (500 m) benefits from short recurrence periods and provides daily coverage of many parts of the globe since February 2000. The 6th version of the MOD09A1 surface reflectance products were used, where each pixel is selected within an 8-day window to provide a composite image with the best observation in terms of low viewing angle, reduced clouds and cloud shadow presence and minimal aerosol loading. 1043 MODIS images from the h16v07 path/row over 2000–2022 were treated here.

The European Space Agency's (ESA) Sentinel-2 A and Sentinel-2B satellites provide multispectral imagery in the 10 m and 20 m bands since 23 June 2015 and 7 March 2017, respectively, over our region of interest. The satellites have a 10-day revisit frequency offset by 5 days, leading to image availability every 5 days since 2017 when combining both sensors. Imagery from European Space Agency's (ESA) constellation of Sentinel-2 satellites were accessed via GEE (asset $COPERNICUS/S2\_HARMONIZED$). Level 2 surface reflectance products are not available until 16 December 2018 in GEE for our ROI but Level 1C products have successfully been used in recent water studies (Yang et al., 2020; Ogilvie et al., 2020a). Our region of interest overlaps on tiles T28QDD, T28QED, T28PFD, T28QFD captured on the same day and 3 tiles (T28PGC, T28PGB, T28PHB) with images 2 days later. Mosaics combining images acquired over a 5-day interval were therefore created to combine these observations. 500 S2 mosaics over 2016–2022 were created.

Images from the TM sensor aboard Landsat 5, the ETM+ sensor aboard the Landsat 7 satellite, and the OLI sensor on Landsat 8 were used in this study. These sensors have similar characteristics providing multispectral imagery at 30 m spatial resolution, at a 16-day time interval, since 1984 for Landsat 5. The combination of imagery from Landsat 7 and Landsat 8 satellites can reduce repetitivity to eight days after 2013 thanks to the eight-day offset between their acquisitions. Imagery from OLI-2 aboard Landsat 9 were not exploited in this long-term study considering that image acquisition began only in autumn 2021. These surface reflectance products are available through Google Earth Engine (assets $LANDSAT/LT05/C02/T1\_L2$, $LANDSAT/LE07/C02/T1\_L2$ and $LANDSAT/LC08/C02/T1\_L2$). Tiles of the following paths and rows were used: 204 48, 204 49, 203 49 203 50. Tiles situated on the same paths are overpassed on the same day, while row 204 is covered 7 days after 203. Mosaics for each sensor were created to exploit all imagery within a 16-day interval. Landsat 7 and 8 mosaics were offset by 8 days based on the 8-day time gap between acquisitions over the same area. 158 Landsat 5 (since 1984), 482 Landsat 7 (since 1999) and 223 Landsat 8 mosaics (since 2013) were created.

2.2.2. EO classification of flooded areas and GEE

The Modified Normalised Difference Water Index (MNDWI) (Xu, 2006) was used to detect water pixels and classify flooded areas. The index was shown (Li et al., 2013; Ogilvie et al., 2015, 2018, 2020a) to provide the greatest accuracy in detecting water in mixed environments (water, flooded vegetation, shallow waters) compared to other commonly used indices. In floodplains, as in wetlands and shallow water bodies, the presence of flooded vegetation (reeds, scrubland, trees) can be important. The stability of the MNDWI threshold over time and locations compared to indices including NDWI and NDVI (Ji et al., 2009; Ogilvie et al., 2018) also increases its suitability when applied to long term studies of water dynamics. The EO imagery geoprocessing chain to obtain binary rasters and estimates of flooded surface areas is detailed in Ogilvie et al. (2020a). Research on a subset of the floodplain around Podor (2000 ha) involving substantial ground truth data and very high-resolution imagery UAV between 2016 and 2019 had enabled the calibration of the index thresholds for each sensor used here. Cloud and shadow masks were generated here to (i) remove the pixels affected by clouds on each image, (ii) assess the percentage of clouds over the ROI. Masks were processed in GEE based on the quality assessment (QA) bands provided with each image. For USGS Landsat Collection 2 imagery, QA bands are produced with CFMask, for Sentinel-2 imagery these are based on SEN2COR and for MODIS these are provided by the MODIS Adaptive Processing System. A USGS gap-fill method was used to account for the SLC-off problems with Landsat 7 ETM+ imagery after 2003. Codes were developed in GEE to apply the approach on the entire image collection for each sensor and export the water, cloud and shadow surface areas over our area of interest for each mosaic image. Images with more than 20% clouds over our ROI were removed here and time series were checked manually to remove aberrant values related to undetected cirrus clouds notably. This approach was chosen to evaluate the actual presence of clouds over our ROI and not unnecessarily remove images where clouds obscure pixels outside of our ROI. R and QGIS were used to analyse and exploit the raster and .csv outputs from GEE.

2.3. FBAS field observations across the floodplain

Field surveys were carried out during the 2022 flood to acquire ground truth data along the Senegal floodplain against which to evaluate the accuracy of the classified areas. These were contained in eight sections of the floodplain between Bakel and Podor in Senegal (Fig. 1) to provide a cross section of areas across the floodplain where recession crop farming is carried out. The surveys identify 64 locations which had been flooded and used for recession crop farming and 56 nearby areas which were not flooded. Locations were captured using GPS and unmanned aerial vehicle (UAV) imagery and were selected to be located within an area at least 30 m by 30 m to be coherent with the size of the classified Landsat and Sentinel-2 pixels (see Fig. 2). Flooded pixels were carefully chosen to be outside permanent water bodies as the difficulty here lies in correctly identifying temporarily flooded areas. Likewise, non flooded pixels were chosen on the periphery of flooded areas, as classification difficulties lie in the fringe areas. These non flooded pixels were chosen outside of areas used for recession crop farming, as these indicate that they were flooded at some point during the season. Confusion matrices to assess the performance of the classification algorithm were used. These assess the agreement between predicted and observed classes, i.e. the ability of EO data to correctly detect flooded and non flooded pixels. Commonly used pixel based accuracy metrics were calculated within R: overall accuracy, producer accuracy, user accuracy, and Kappa coefficient. Producer accuracy (Prod. Accu) and user accuracy (User Accu.) values are important to interpret overall accuracy values as they inform about omission and commission errors, respectively. These well-known metrics are explained in Stehman and Foody (2019), Li et al. (2018).

Fig. 2. Example of sorghum plots in the Senegal river floodplain surveyed with GPS and unmanned aerial vehicle (UAV) imagery.

In addition field data gathered in 2018 in the Podor floodplain was used. Using a handheld GPS, 446 plots used for flood-based agriculture following the 2018 flood were surveyed and delimited. This data is exploited here to analyse the duration of the flood across these plots and provide insights into the water requirements for flood-based agriculture.

2.4. Global water data sets

Global Surface Water (GSW) datasets produced by Pekel et al. (2016) were also used for comparison. These exploit the Landsat 5, 7 and 8 archives to provide, based on a combination of expert systems, visual analytics and evidential reasoning, what is often regarded as the most advanced and detailed surface water datasets at a 30 m resolution (Huang, 2018). All available monthly images from the GSW datasets for 1999–2021 available within Google Earth Engine (asset $JRC/GSW1\_4/MonthlyHistory$) were processed to extract monthly surface water values for our region of interest. The flood dynamics obtained by GSW were compared here with those obtained by Landsat, Sentinel-2 and MODIS, as well as with the hydrological flow data at Bakel. The flood occurrence maps produced by the GSW datasets (asset $JRC/GSW1\_4/GlobalSurfaceWater$, band $occurrence$) from imagery over 1984–2021 was also extracted for the ROI and compared through visual interpretation with the multi-year occurrence maps produced in this work.

2.5. Hydrological data and regression models

Monitoring of stage levels of the Senegal River has been carried out since 1904 at Bakel and is currently managed by the DGPRE (Direction de la Gestion et Planification Générale pour la Protection des Ressources en Eau, in French) in Senegal in collaboration with the OMVS (Organisation pour la Mise en Valeur du Fleuve Sénégal). Early data contain more gaps and uncertainties, therefore the corrected datasets produced by IRD for the Actualisation de la monographie (Bader, 2015) were used here. These provide flow data based on updated stage-discharge rating curves. Daily flow measurements over 1950–2022 from Bakel gauging station on the Senegal river were exploited, and averaged into monthly and yearly flow values.

2.5.1. Comparing annual flood amplitudes from EO and hydrological data

Hydrological data was used to explore the coherence of the annual peak flooded areas estimated through EO in the Senegal floodplain against flow data from the upstream Bakel gauging station over 2000–2022. The Bakel station is a strategic station for this, as it is situated downstream of the major tributaries: Bakoye, Falémé and Bafing and is therefore representative of the total flow transiting through the floodplain. Correlations were explored between monthly peak flow and peak surface areas detected by all five EO sources (L5, L7, L8, MODIS, S2) and GSW global surface water datasets. R-squared (R^2), a standard goodness-of-fit measure was used to evaluate the correlation. Correlations were investigated using peak monthly flow data instead of peak daily data, as the extent of inundated areas is determined by both the amplitude and the duration of the flood pulse (Bader, 2015) as illustrated by the flow hydrographs (Fig. A.2). For example, the prolonged peak observed in 2020 (QJ_{max} = 3464 m^3/s, QM_{sept} = 2854 m^3/s) leads to a greater flooded area than the higher, shorter flow pulse measured in 2019 (QJ_{max} = 4956 m^3/s, QM_{sept} = 2400 m^3/s).

2.5.2. Modelling historical variations in the floodplain

Relations between hydrological data of the Senegal river and earth observations of flooded areas were further explored to derive the optimal numerical model equations which can be used to estimate peak flooded areas based on hydrological observations. Considering the difficulties in modelling floodplains due to digital elevation model (DEM) uncertainties across these large, flat alluvial plains, several works have focussed on developing statistical regression models to relate variations in stage or flow in the river with water surface areas in the floodplain As shown in previous studies of large rivers (Ogilvie et al., 2015; Orieschnig et al., 2022), the amplitude of large floods which are generated by rainfall upstream are well correlated with the amplitude of flow in the river bed upstream. These regression models can then be fed into 1D models or water use models for planning purposes as done in the Niger river (Ogilvie et al., 2015; Seidou et al., 2021; Jung et al., 2011; Orieschnig et al., 2022; Padi et al., 2011). In the Senegal river, the existing relationship developed on the basis of 7 SPOT images in the 1990s remains used to model future changes in the extent of the flooded areas under the influence of upstream changes, notably dam operations (Bader et al., 2003; Tilmant et al., 2020; SCP et al., 2009; BRLi et al., 2021).

Regression models were explored using monthly flow data at Bakel for 2000–2022 averaged over different months of each year. Maximum monthly runoff (Qmeanmax) and average runoff over two and three months to identify which month(s) could be best suited to estimate or predict the flooded areas based on flow data upstream were investigated. Based on Fig. A.2, mean runoff per year for the highest month, for the months of August, September, October and for their bimonthly and trimonthly means were used to investigate correlations, i.e. QM_{max}, QM_{aug}, QM_{sep}, QM_{oct}, $QM_{aug-oct}$, $QM_{aug-sep}$ and $QM_{sep-oct}$. Regressions were explored using a 60–40 split sample approach (Motavita et al., 2019), where data from 60% of the years were used to calibrate the equations-models and the other 40% were used for validation. The 23 years (2000–2022) were therefore split into two periods: 2000–2012 and 2013–2022 for validation. Both periods considered including very wet years (2003, 2020) and dry years (2006, 2017) but in other cases methods such as sliding window techniques or differential split sample tests (Dakhlaoui et al., 2019) may be used to ensure a range of hydroclimatic conditions. MODIS earth observations were used here as they provide a reliable time series over 20 years (vs 7 years for S2). The amplitude of the annual flood peaks detected by MODIS over 2000–2022 were bias corrected based on the near systematic underestimation (R^2 = 0.99) of MODIS compared to S2 over 2016–2022 using the following equation:

$$S_{max\_S2} = 1.1336 * S_{max\_MODIS} \quad (1)$$

where S_{max_S2} and S_{max_MODIS} are the annual peak water surface areas detected by Sentinel-2 and MODIS imagery respectively. Linear polynomial models were calibrated and evaluated based on standard performance metrics between the peak surface area predicted by the model and peak surface area estimated from earth observations. Nash–Sutcliffe Efficiency (NSE) and Kling–Gupta Efficiency (KGE) which combine the three components of model errors (correlation, bias, ratio of variances or coefficients of variation; Liu 2020) were used.

The regression model with the strongest performance is then calibrated on the full time series of 23 years of bias-corrected MODIS observations and flow data. The definitive numerical model is finally applied to the long term time series of data from the Bakel gauging station available for 1950–2022 to model past variations in flooded areas in the Senegal floodplain. The 73 years of observations are then used to calculate quantiles and converted into exceedance probabilities, i.e. indicating the surface areas flooded at least 1%–99% of the time. Quantiles are calculated over 1950–2022 as well as over three periods corresponding to the high flow years (1950–1971), the great drought (1972–1993) and recent times (1994–2022) where rainfall and flow recovered somewhat Bodian et al. (2020), Descroix et al. (2020).

2.6. Estimating flood based agriculture in the floodplain

2.6.1. EO multi-year flood occurrence maps

Earth observations of flooded areas were aggregated to create composite flood occurrence maps. The classified rasters mosaicked over the whole floodplain for each 5 or 8 day period were aggregated for each year and over several years in GEE. Filters were used to select images between September and November when the river overflows into the floodplain and thus exclude areas which are flooded for other reasons notably irrigated perimeters. Fieldwork in the Podor floodplain confirmed that even in high flood, waters had receded at the end of November in areas used for recession crop agriculture. Cloudy pixels were masked when creating the mosaics on each date but additional filters are applied in posttreatment to remove their residual presence based on a minimal threshold. Visual interpretation is first used to identify the range of values of residual cloudy pixels, i.e. pixels classed as flooded outside the floodplain resulting from cloud and shadow interferences. Accuracy values are then evaluated for varying thresholds in increments of 2 within this range (here 1–21) and pixels below the threshold which maximises overall accuracy are excluded. These products provide maps of the duration pixels are flooded, which are analysed to appreciate the amount of land in the floodplain which is suitable to flood recession agriculture. Applied to the full time series of observations, this approach creates a multi-year occurrence map which also provides a mask at 20 m of permanent water bodies and temporary flooded areas that are relevant to FBAS.

2.6.2. Regression model of FBAS cropped areas

Data to characterise the extent of flood recession agriculture in the floodplain were compiled from available literature and national data sources. Crops grown in the floodplain consist essentially of sorghum, maize, cowpea and to a lesser extent melon and watermelon (Poussin et al., 2020; Sall et al., 2020a). Data for the period 1950–2000 were extracted from Lamagat (2001). This work had compiled, analysed and criticised observations and statistics data over the period 1946–2000 on recession crop farming on both the Senegalese and Mauritanian banks of the Senegal river floodplain. Based on this data, Lamagat (2001) identified a relationship with estimates of the flooded surface area and secondly with river stage data at Bakel. Despite the simplifications inherent to this approach which does not model socio-economic changes or livelihood changes, this relationship remains an essential tool for the river basin agency (OMVS) in the operational management of the Manantali dam as well as in its long term strategic planning (Bader et al., 2003; SCP et al., 2009; BRLi et al., 2021). This regressive model is here updated based on the flooded surface area that we obtain from our approach. Considering the complex relation between flooded areas and cropped areas developed by Bader, which led to a specific equation below 80,000 ha cropped and over, natural spline smoothing is used. This is a powerful regression method which builds a piecewise polynomial function, therefore fitting a different polynomial curve for different ranges of flooded areas. The model was calibrated on the 18 years where observations are available and then applied over 1950–2022 to provide an estimate of areas cultivated in recession farming. Quantiles and exceedance probabilities are calculated to analyse and discuss the dynamics in cultivated areas. For recent years, annual statistics are hard to obtain considering the emphasis placed on irrigated crops and the large, transboundary scale of the floodplain. Statistics gathered by national authorities in Senegal provide data on the number of households involved in flood based agriculture but not associated surface areas sown and production levels (ANSD, 2014). Cropped areas and production levels are however available per department for major crops per department (DAPSA, 2021). Data on key FBAS crops including sorghum, millet and cowpea are exploited here to estimate surface area cropped in part of the floodplain and discuss the relevance of the results from the regression model.

3. Results and discussion

3.1. EO mapping and monitoring inundated areas in the Senegal floodplain

3.1.1. Multi-year flood dynamics from EO sensors vs. hydrological data

Flood dynamics obtained from earth observations are illustrated for each satellite in Fig. 3. Though Landsat 5 TM and GSW provide observations since 1984, results highlight how the limited availability of images until 1999 leads to clear difficulties in monitoring flood dynamics. Following the launch of Landsat 7, observations are reliably acquired on the entire globe every 16 days but results point to ongoing difficulties in capturing the flood dynamic, as seen in the absence of a coherent flood pulse with clear flood rise and decline phases, and a marked flood peak (Fig. A.3). The lower correlation metrics between peak flooded areas detected by Landsat observations and the peak monthly flow in the Senegal river (Fig. A.5) confirm these difficulties to reliably capture the flood peak, and outliers point to underestimations certain years (e.g. 2009, 2018). Landsat 8 imagery for the floodplain provides enhanced possibilities to monitor the flood dynamics partly by removing uncertainties through improved high (cirrus) cloud detection with the Band 9 as well as narrower spectral bands, but the 16 day interval between acquisitions leads to underestimating some annual peaks.

Sentinel-2 and MODIS, despite its 500 m resolution, allows for an effective, coherent monitoring of the flood dynamic over time, partly due to the increased temporal repetitivity. The high correlations between upstream flow values and peaks water surface areas detected by S2 and MODIS imagery point towards an accurate detection of the peak flooded areas, at least in relative terms, as their amplitude are shown to vary accordingly to the amplitude of river flows. Water surface areas estimated from S2 observations are close to those obtained from MODIS observations (Fig. A.4) but peaks are consistently higher (by 13%, Eq. (1)), which is coherent with the finer spatial resolution of Sentinel sensors. The 20 m resolution also allows a better understanding of the flood recession phase thanks to the increased detection of small flooded areas visible in Fig. A.4. In 2022, greater cloud presence during the flood led to more scattering in the results from Sentinel-2.

Table 1
Accuracy metrics calculated for MNDWI classification of flooded areas on Landsat 7, Landsat 8, Sentinel-2 and MODIS imagery against 2022 ground truth.

Satellite	Producer accuracy	User accuracy	Overall accuracy	Kappa
Sentinel-2	0.89	1.00	0.94	0.88
Landsat 8	0.91	0.97	0.93	0.87
Landsat 7	0.91	0.92	0.91	0.81
MODIS	0.76	1.00	0.87	0.75

3.1.2. Pixel based accuracy assessment of EO classifications of inundated areas

Table 1 summarises the accuracy metrics of the confusion matrix comparing the resulting maps of water areas from each satellite source against extensive ground truth data acquired along the floodplain in 2022. Overall accuracies are high especially with Sentinel-2 and Landsat 8 partly as a result of their high spatial resolution. Fig. 4 illustrates the capacity of these earth observations to correctly classify dry ('not flooded') and wet ('flooded') pixels in this heterogeneous environment. MODIS accuracy metrics are lower due largely to the lower spatial resolution (463 m). Fig. 4 illustrates the omission errors (the central ground truth points) resulting from the lower spatial resolution and the difficulties to correctly capture smaller flooded areas, notably small channels and meanders that were then used for recession cropping in 2022. These errors are reflected in the lower producer accuracy but user accuracy is optimal indicating that calibration of the MNDWI threshold here prevents overestimation of flooded areas and overall accuracy remains good despite the lower spatial resolution at 0.87%. Landsat 7 performs less well than Landsat 8, in part due to the scan line corrector problems after 2003 which are filled through interpolation and therefore reduce the level of detail and precision, potentially masking isolated land or water pixels, as illustrated in Fig. 4. GSW imagery is not available for 2022 so could not be used in the pixel-based accuracy assessments. These results confirm the relevance and accuracy of the MNDWI classification of flooded areas and confirm that the high goodness of fit coefficient obtained in the previous section do not mask a systematic under or overestimation of surface water areas.

3.2. Modelling flooded area from upstream flows

Table 2 summarises the accuracy and performance indicators for each of the regression models which seek to estimate flooded areas based on monthly flow values over different periods in calibration and validation phase. Strong correlations are observed between the monthly maximum flow and maximum flooded areas but the relationship can be further improved by considering the mean flow over August–September each year. Taking the mean flow over the two highest months improves the coefficient of determination NSE and KGE from 0.64 to 0.84 in validation phase. Peak flow occurs between August and October at Bakel (Fig. A.2) and including October monthly flow improve marginally upon this correlation, with a 0.01 point increase in both NSE and KGE. The timing of the peak flow depends on rainfall in the upstream catchments but also the amplitude of the flood. At Bakel the peak flow is generally reached during September but occasionally mean August flow can be superior as occurred during lower floods in 2011 and 2021.

The most robust approach is then used to define the linear model based on the full 23 years of MODIS observations and flow data. The definitive correlation curve is shown in Fig. 5 and defined in the following equation:

$$S_{max} = -1.745 * 10^9 + 3.576 * 10^6 * Q_{mean8910} - 345.5 * Q^2_{mean8910} \quad (2)$$

where S_{max} is the annual peak water surface area in the floodplain in m^2 and $Q_{mean8910}$ is the average flow over August–October at Bakel in m^3/s.

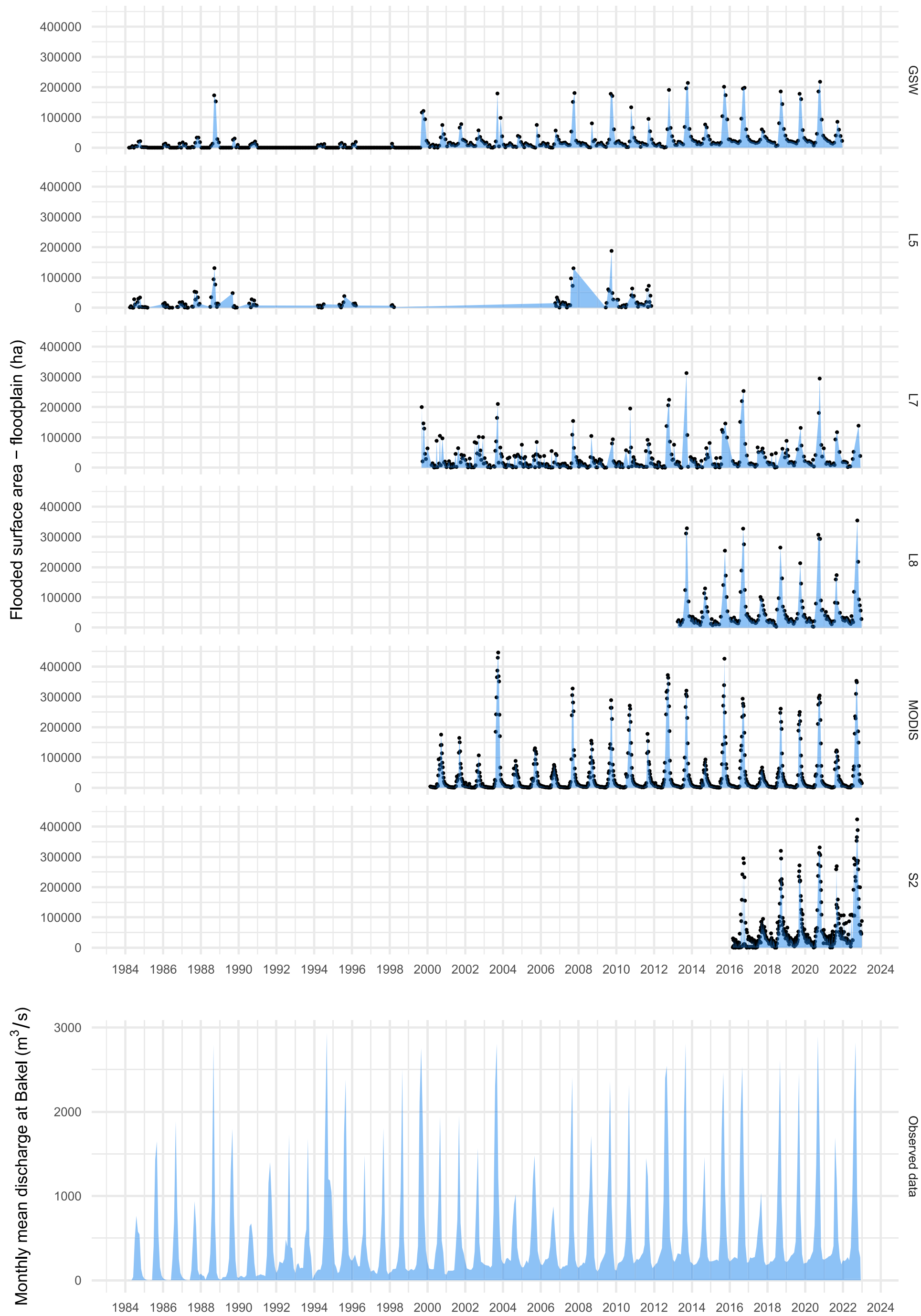

Fig. 3. Flooded surface area across all areas over full available period based on 6 satellite sources compared with monthly runoff in the Senegal river at Bakel gauging station over 1984–2022.

3.3. Historical variability of flooded areas

Based on the results obtained above, the variations in flooded area were modelled since 1950 (Fig. 6). Water surface areas display stark variations over time, ranging from 30,000 to 720,000 ha. The average flooded area over the whole 1950–2022 reaches 329,000 ha but clear phases are observed in line with the high variability of the hydrological regime of the Senegal river since 1950 which typically distinguishes three phases (Bader, 2015; Bruckmann et al., 2022). Fig. A.1 illustrates the stark difference in average annual discharge at Bakel, with high flow during the 1950s and 1960, followed by the very dry years of the great drought in the Sahel from 1974, and a relative return to higher flow years since the mid 1990s.

Peak flooded areas exceeded 600,000 ha ten times and reached an average of over 553,000 over 1950–1971 (Fig. 7). In terms of peak monthly flow, historical data reveals maximum values reaching over 8000 m^3/s in early September 1950, and over 4000 m^3/s when averaged over August-October 1950. On only two occasions over this period did average flow on August-October fall below 2000 m^3/s. Over 1972 to 1993, the average flooded area per year remained under 200,000 ha (196,000 ha) and on four occasions below 50,000 ha (1983, 1984, 1987, 1990). During this period mean flows over August-October remained under 2000 m^3/s with the exception of 1974. Since 1994, flooded areas have recovered somewhat but remain highly variable, reaching over 300,000 ha during good years (13 years over 1994–2022) but below 100,000 ha on four years (1996, 2004, 2006, 2017),

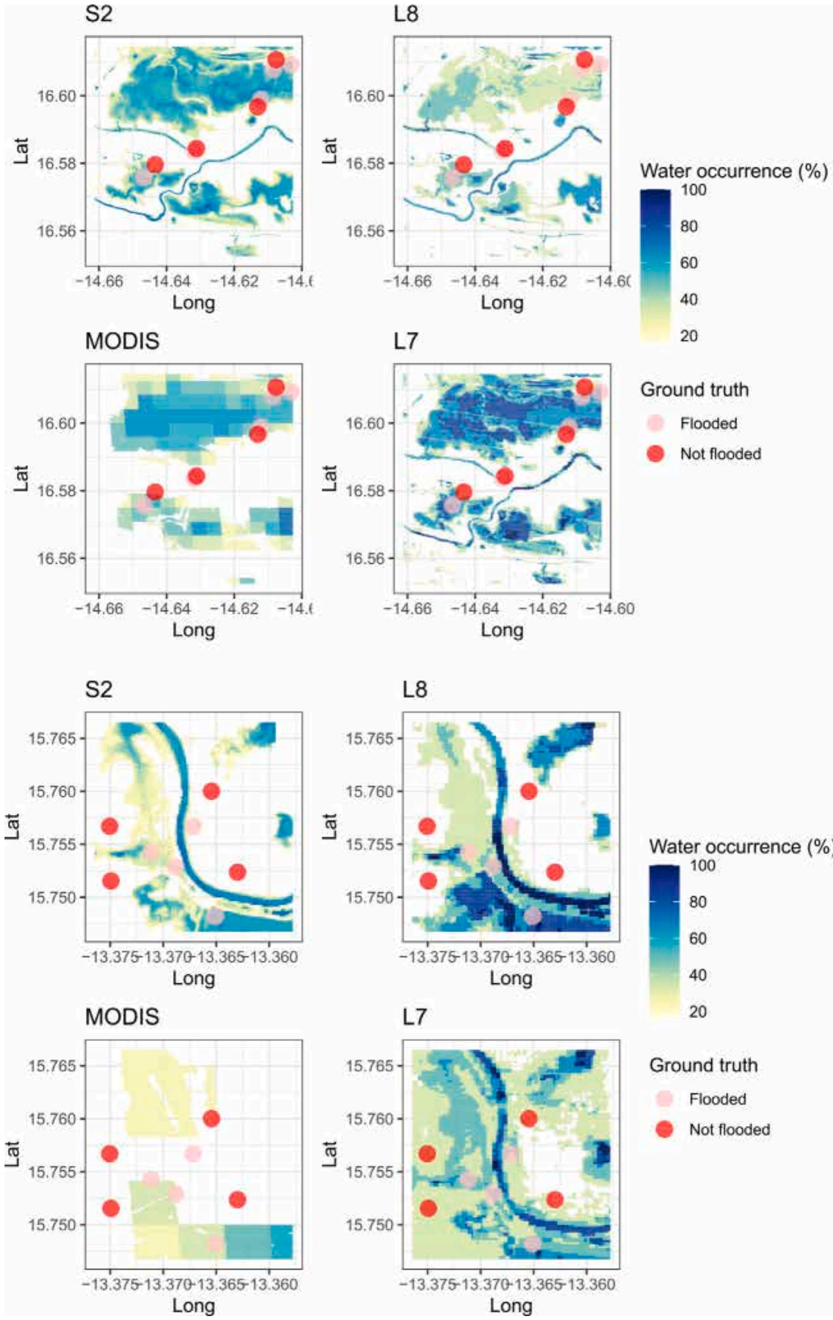

Fig. 4. Comparison of flooded areas detected by four EO sensors for 2022 against ground truth in two locations.

Table 2
Performance metrics of the linear models estimating flooded areas based on monthly flow at Bakel over different periods.

Flow data source	Calibration		Validation	
	NSE	KGE	NSE	KGE
QM_{max}	0.96	0.97	0.56	0.64
QM_{aug}	0.77	0.83	0.36	0.69
QM_{sep}	0.94	0.96	0.58	0.62
QM_{oct}	0.51	0.59	0.32	0.68
$QM_{aug-oct}$	0.91	0.93	0.81	0.85
$QM_{aug-sep}$	0.96	0.97	0.80	0.84
$QM_{sep-oct}$	0.86	0.90	0.62	0.70

leading to an area of 260,000 ha exceeded 50% of the years over this period (Fig. 15). Flooded areas exceeded 95% of the years over each period varied from 400,000ha, to 37,000 ha before recovering partly to 89,000 ha. This is mirrored in the flow data where mean flows over August-October have recovered partly exceeding 2000 m^3/s on good years.

The absolute values for several years (in grey in Fig. 7) before 1975 are subject to greater uncertainty as several values before 1975 are for mean flow values outside the range the model was developed upon. As Fig. 6 emphasises the model was calibrated-validated upon average monthly flows over Aug–Sep under 2200 m^3/s. Unlike linear relations, the quadratic polynomial regression used here does however lead to a slower increase at the high end of the range, potentially limiting overestimation errors. Values obtained here correspond to peak flooded areas, i.e. synchronously flooded areas, as opposed to the sum of areas flooded at some point during the flood. Over 2022, total flooded areas reaches 433,000 ha vs a peak flood of 424,000 ha. This indicates that

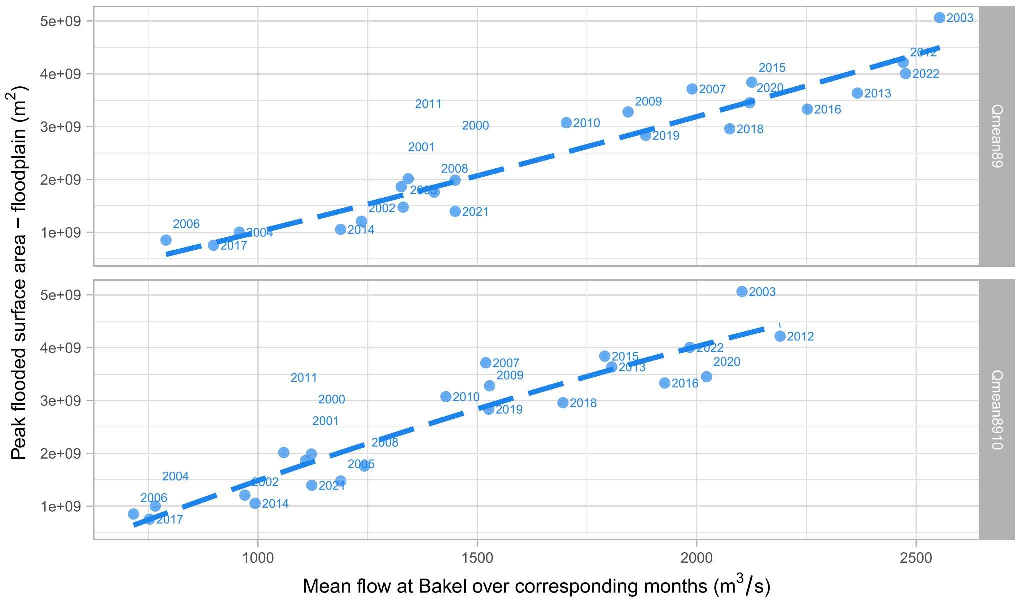

Fig. 5. Correlation between peak flooded area in the floodplain and mean flow at Bakel over aug–sep and aug–oct respectively).

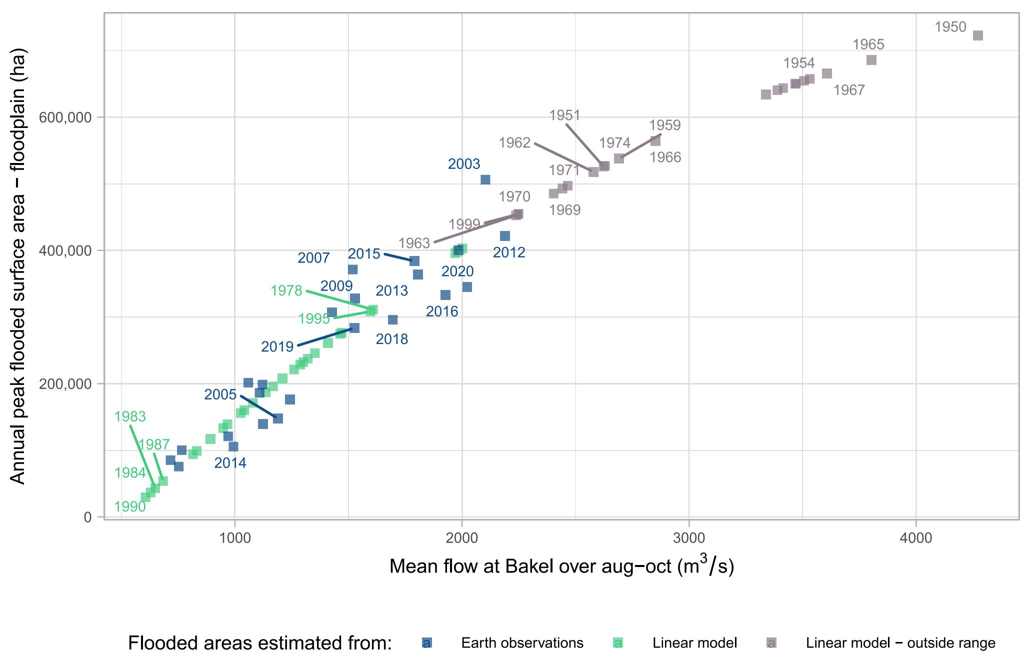

Fig. 6. Estimated peak flooded areas based on earth observations and modelled based on Bakel flow data over 1950–2022.

despite the scale of the floodplain the peak is concomitant across the floodplain i.e. when the south is flooded the north is still flooded (even if only marginally).

3.4. Supporting flood based agricultural systems

3.4.1. Mapping water occurrence and potential for FBAS

Fig. 9 provides an overview of the produced multi-year water occurrence map, and Fig. 10 a close-up view of the flooded areas at 20 m resolution. The high resolution mask provides a coherent connection between flooded areas, reproducing small channels and meanders seen in the Sentinel-2 true colour composite imagery.

Field observations in the Podor floodplain of the areas effectively cropped in 2018 were compared with the 2018 flood occurrence map. Fig. 10 highlights the accuracy of the map in detecting temporarily flooded areas used for FBAS that year. It also illustrates how much of the flood based agriculture is concentrated on the periphery where the flood duration is lower. The density distribution plot (Fig. 11) reveals that the greatest proportion of land used for FBAS was flooded 40 days (median 42 days, s.d. 15 days) and that 80% of land cropped is flooded between 19 and 57 days. Annual occurrence maps for 2017–2022 were created from S2 observations and Fig. 12 summarises for each year the surface area in the floodplain flooded for varying durations of time over September–November. The areas in green on Fig. 12 isolate the areas which are flooded between 19 and 57 days and are potentially suitable for FBAS.

In good years such as 2018, 2020, 2022, we estimate that near 200,000 ha in the floodplain were flooded for this duration of time and therefore could be suited in hydrological terms to FBAS. In low flood years such as 2017, just under 50,000 ha were flooded, illustrating the

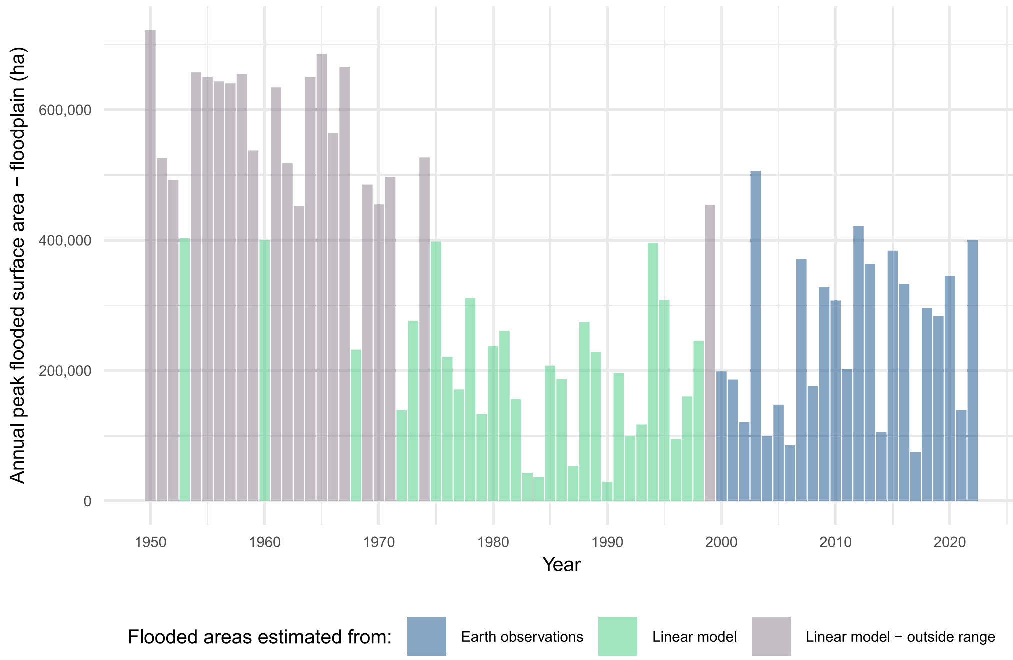

Fig. 7. Annual maximum flooded surface area estimated based on earth observations and regression model for 1950–2022.

Fig. 8. Image from Papy (1951) of the floodplain at Rosso looking towards Mauritania during the high flood, 18.10.1950.

impact of lower amplitude floods on FBAS. The effect of prolonged floods is also clearly visible on the flood duration plots, where the prolonged periods of flows above 2500 m^3/s in 2020 (Fig. A.2) is shown to have produced a more prolonged flood than in 2022.

3.4.2. Modelling recession flood cropping in the floodplain

The correlation between flooded areas and recession cropping are shown in Fig. 13 updated here based on the results from our approach. These lead to estimating for the past 72 years the estimated extent (ha) of recession farming practised in the floodplain based on the flooded surface areas detected from the earth observations. Fig. 14 highlights that cultivated area vary between from just over 10,000 ha to over 100,000 ha over 1950–2023. Values of 100,000 ha were regularly exceeded during the 1950s, nearly 75% of the time until 1971 (Fig. 15) but since 1974 this values is estimated to have been reached only once. Since 1994 and the return of larger flooded areas, the average recession crop area is estimated to 57,000 ha but variability is high with an alternation of years where cropped area reach over 75,000 ha and years under 40,000 ha.

Fig. 13 points to a modest rise in cultivated areas for flooded areas up to 200,000 ha which appears consistent with observations in the (Podor) floodplain and the fact that areas most regularly flooded include land where natural vegetation thrives and hinders cultivation. These are also areas where water may remain for extended periods in temporary ponds and are therefore not suited to recession cropping which must begin sufficiently early in the growing season. Once floods increase over 200,000 ha, flood waters reach some of the most suitable land in the floodplain and the increase per ha flooded is more significant. Field observations during 2022 confirmed the significant land areas turned into recession crop farming following the large flood. Above 500,000 ha of flooded land, the rise in cultivated area per hectare of flooded land declines. This may partly be due to the fact that part of the land flooded in these extreme high waters includes non agricultural land, e.g. roads, urbanised areas (as seen in illustrations in Papy (1951)), and includes areas which are not regularly used for flood recession cropping. Fig. 13 also points to the fact that Lamagat (2001) in the POGR modelled larger cultivated areas for flooded areas under 300,000 ha, apparently giving less weight to observations over 1976–1979 and 1994.

4. Discussion

4.1. Monitoring surface water dynamics in floodplains with earth observations

By exploiting a site-specific MNDWI classification approach suited to shallow, mixed water environments and the full archive of MODIS, Landsat, Sentinel-2 satellite imagery, up to 135 000 ha additional flooded areas in the Senegal river floodplain are detected compared to Global Surface Water (GSW) data sets (Pekel et al., 2016). Accuracy assessments in Ogilvie et al. (2020a), carried out on a subset of the floodplain against ground truth data consisting of high resolution DEM, limnimetric measurements and unmanned aerial vehicle (UAV) imagery, previously established that GSW led to greater errors (RMSE = 228 ha, NSE = 0.69) and underestimations in the peak flooded areas. These omission errors are here clearly propagated at the scale of the whole floodplain and confirm previous concerns about GSW's suitability to detect non-pure pixels where vegetation and water reflectance mix (Aires et al., 2018; Yamazaki and Trigg, 2016; Hardy

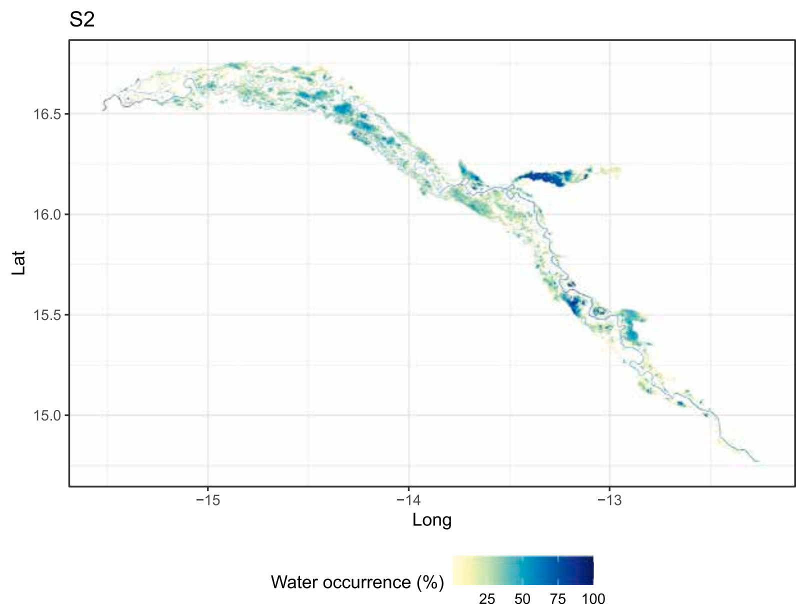

Fig. 9. Overview of Sentinel-2 multi-year flood occurrence map.

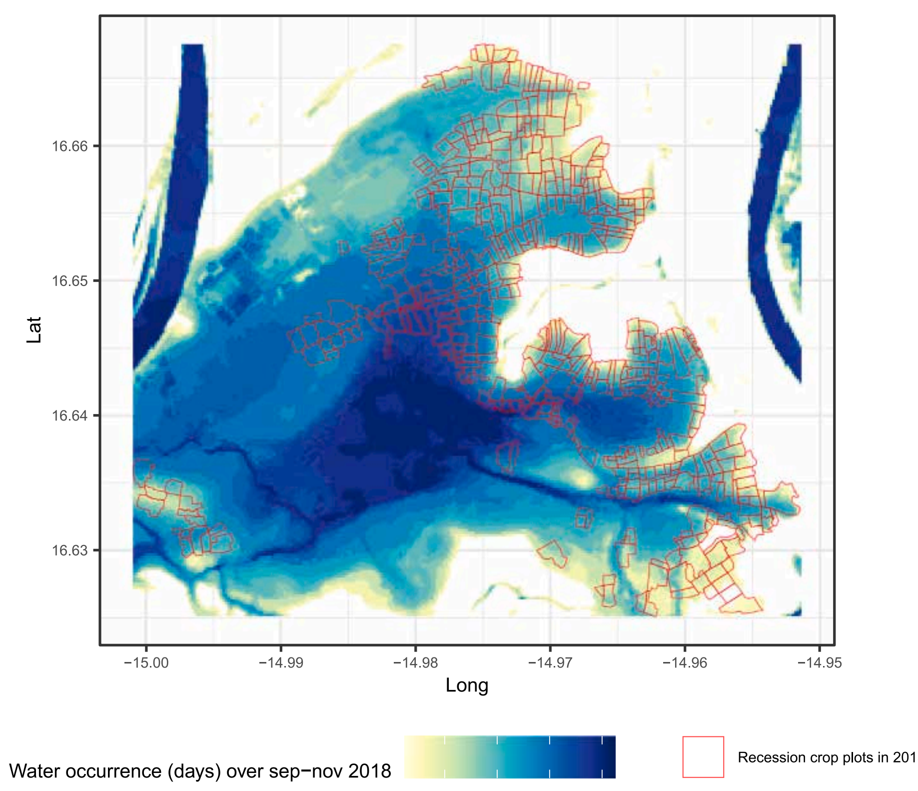

Fig. 10. Water occurrence over sep–nov in 2018 for 464 FBAS plots surveyed in the Podor floodplain.

et al., 2019; Herndon et al., 2020). Furthermore, despite providing data since 1980s, GSW which combines observations from Landsat imagery sources suffers from the same difficulties as Landsat 5 until 1999 to reproduce water dynamics in the floodplain (Fig. 3). Using a single image per month, the GSW datasets underestimate the flooded areas after 1999 compared to other sensors, partly as a result of earth observations during high waters occurring up to several weeks after the flood peak. Over 2013–2022 (Fig. A.3), peak flooded areas are estimated around 200,000 ha with GSW data, but reach above 300,000 ha with MNDWI applied to Landsat, Sentinel and MODIS imagery.

Several products in the literature focus on combining multi-source imagery, especially Landsat and Sentinel-2 observations (Yamazaki and Trigg, 2016; Donchyts et al., 2016; Claverie et al., 2018), to monitor water bodies. Results here illustrate the difficulties of Landsat to capture flood peaks accurately due to its temporal resolution, reducing the value of such products before Sentinel-2 imagery. Fusion of multi-source earth observations holds greater potential by combining the benefits of high spatial resolution imagery from Landsat and Sentinel-2 satellites with high temporal resolution MODIS observations. Data fusion methods including STARFM (Gao et al., 2006) and ESTARFM (Zhu

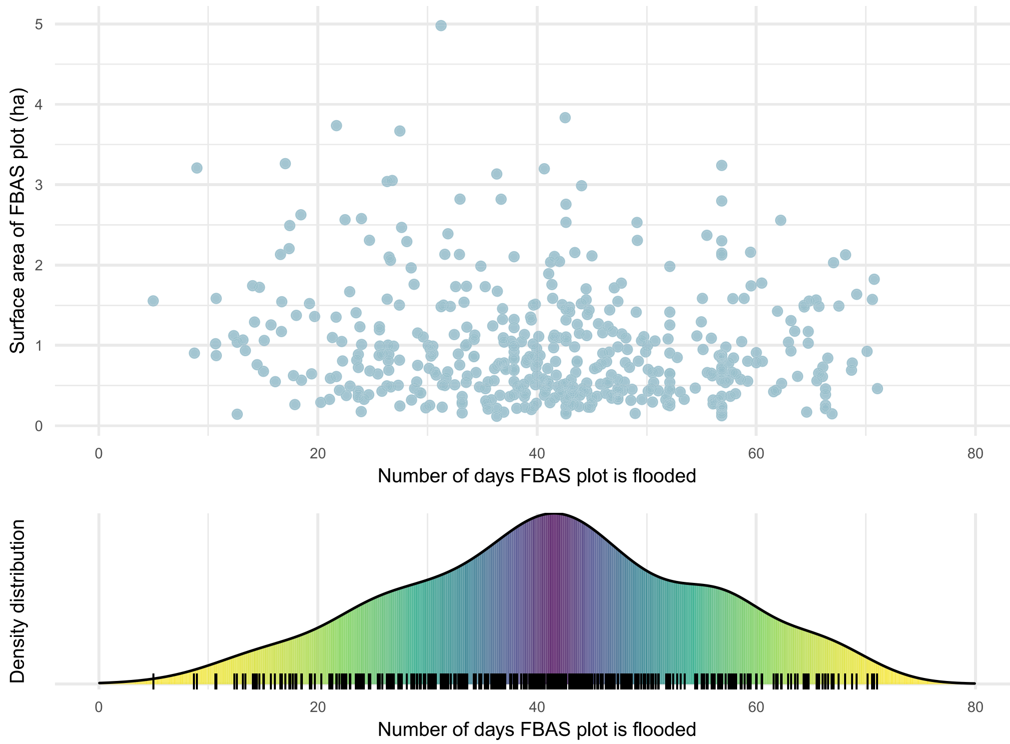

Fig. 11. Density distribution of the duration of the flood in the 464 FBAS plots and scatterplot of the surface area vs. the number of days each plot is flooded.

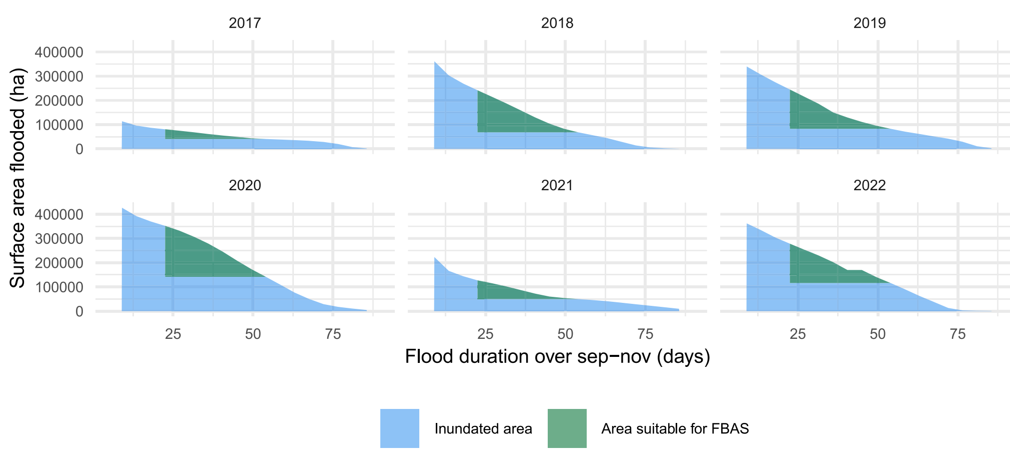

Fig. 12. Length of time surface area are flooded in the floodplain over September–November and proportion of these which areas suited to FBAS based on S2 occurrence maps for 2017–2022.

et al., 2010) are the most widely used. Xiao et al. (2022) notably used ESTARFM to create 25 images from Sentinel-2 and MODIS observations to monitor irrigation dynamics over one growing season, and Heimhuber et al. (2018) similarly generated 8-day resolution maps from Landsat and MODIS imagery to study Australian floods in 2010. However, spatiotemporal fusion (STF) methods remain subject to numerous challenges, including spatial and spectral differences between fine and coarse EO imagery as well the application of STF models (Xiao et al., 2023) especially in long-term and large scale studies. Fusion methods also face difficulties to accommodate sudden changes of land use over time in complex, heterogeneous environments (Htitiou et al., 2021) as observed in such floodplains.

Importantly, results here highlighted the high spatial accuracy (overall accuracy = 0.87) of MODIS imagery despite its moderate spatial resolution and its optimal ability to study long term surface water dynamics (R^2 = 0.87). As in other case studies, MODIS remains essential to explore surface water variations in wetlands and floodplains (Bergé-Nguyen and Crétaux, 2015; d'Andrimont and Defourny, 2018; Aires et al., 2020), as well as on smaller water bodies (Ogilvie et al., 2020a). Considering the poor performance of Landsat 5 observed here (Fig. 3), fusion methods would not have been capable of extending EO observations as far back as 1984. MODIS imagery was therefore used to monitor temporal dynamics over 2000–2022 and to derive long term regression models between discharge and flooded areas that were then used to model flooded areas as far back as 1950. High spatial resolution 5-day imagery from the Sentinel-2 A and 2B constellation were used to map water occurrence and FBAS potential in recent years. In other contexts, such as small water bodies, fusion methods may provide benefits to monitor surface water dynamics at very high spatial and temporal resolution. Results also confirm here the ability of optical sensors to correctly reproduce the flood dynamics, due to the limited cloud presence in this Sahelian floodplain during the rainy season. In other regions, however, the presence of monsoon clouds may require

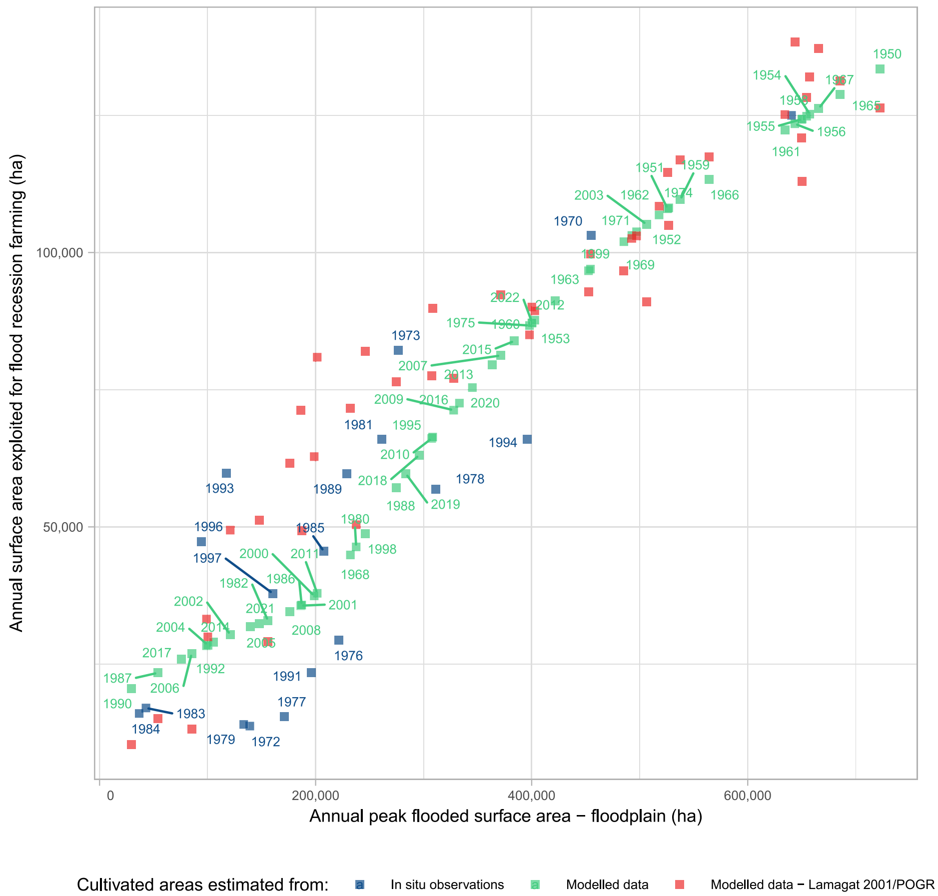

Fig. 13. Relationship between annual peak flooded area and surface area cropped for recession farming.

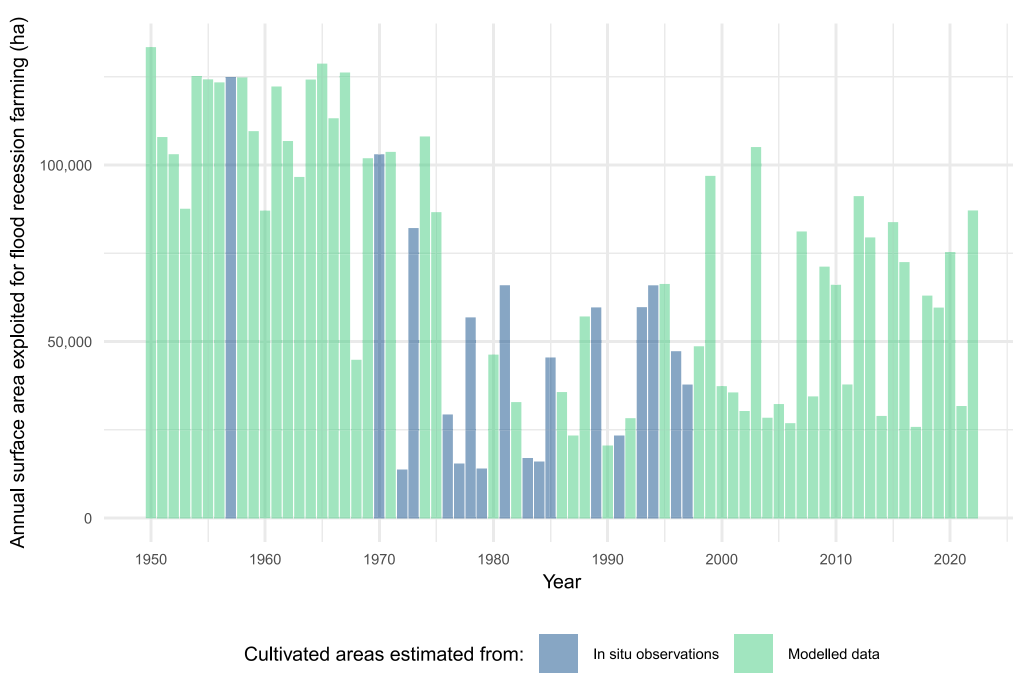

Fig. 14. Surface area exploited for flood recession cropping over 1950–2022 estimated from in situ observations and modelling.

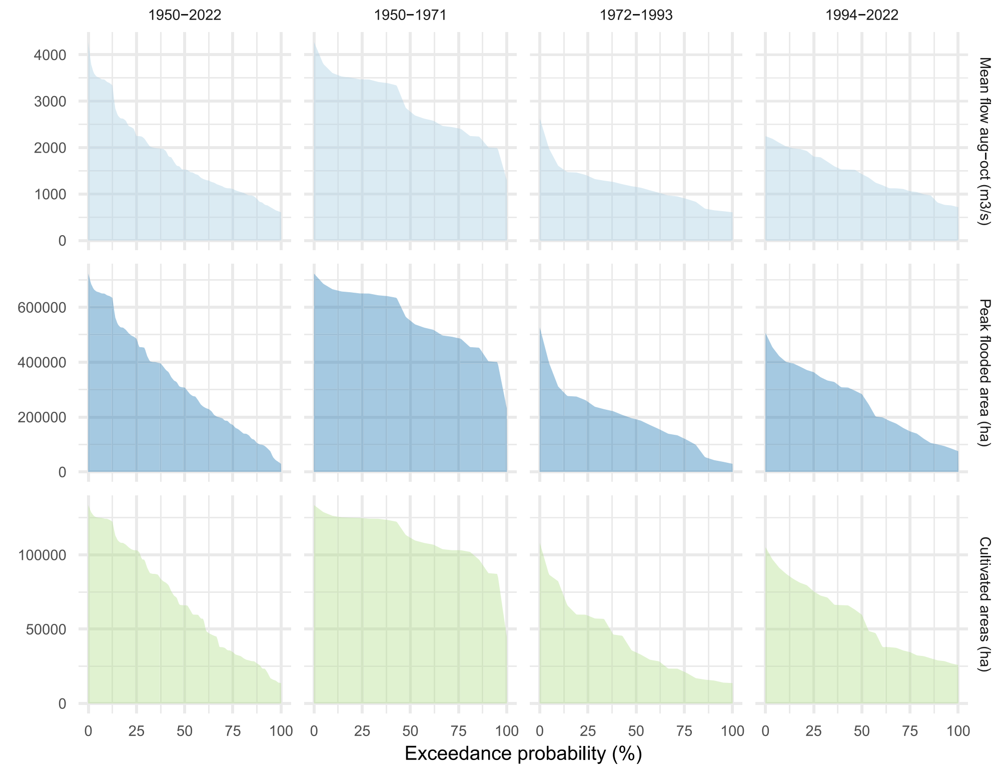

Fig. 15. Exceedance plots indicating the probability that values of mean flow, flooded area and cultivated areas are exceeded for a given year over 1950–2022 and for three sub-periods: 1950–1971, 1972–1993, 1994–2022.

imagery from active sensors such as Sentinel-1 (Mahdianpari et al., 2018; Amani et al., 2019).

4.2. Historical and future trends in flooded areas

Earth observations of flooded areas across the Senegal floodplain over 22 years led to the development of robust regression models (KGE ≥ 0.84) between peak flooded areas and discharge data. These allow the most comprehensive assessment of interannual trends in flooded areas over 1950–2022. Results show that average flooded areas over the whole period reach 329,000 ha but with stark interannual variability already observed in the hydrological regime. The average flooded area declined drastically to 196,000 ha over the dry 1972–1993 period from 553,000 ha during the hyper wet 1950–1971 period. Since 1994, flooded areas have recovered partially to an average of 260,000 ha, supported by the increase in annual rainfall observed by Bodian et al. (2020). Discharge and flooded areas however remain significantly lower to levels reached in the 1950s and 1960s as a result of reduced rainfall and the influence of the Manantali dam put into operation on the Bafing tributary in 1987 (Bruckmann et al., 2022).

In the literature, peak flooded areas in 1999 were previously estimated around 210,000 ha (Lamagat, 2001; Bader, 2015; Bruckmann et al., 2022) vs 454,000 ha in this work. Part of the difference originates from the differences in ROI which here extends upstream of Matam, the inclusion of permanent areas (estimated around 16,000 ha from our Sentinel-2 water occurrence maps) and the improved MNDWI classification discussed previously. Furthermore, regressions based on a limited (7) number of images, that were rarely synchronous with the flood peak according to the authors, were used to extrapolate to other years. Mettrop et al. (2019) estimated a peak of 450,000 ha in 2003 which is comparable with our estimation of 506,000 ha, despite a significantly different approach aggregating flooded areas estimated from stage values at Podor and Matam. Their ROI was limited to 755,000 ha vs 1,100,000 ha, and notably excluded the regularly flooded areas east of Kaedi. Our assessment reveals that the large floods occurring in the 1950–1960s may have flooded in excess of 600,000 ha. Aerial photography of the 1950 flood (Papy, 1951) relate the amplitude of the devastating floods where much of the floodplain was indeed inundated (Fig. 8). 1950 along with 1866, 1871, 1906, 1922, 1927, 1936, were recorded as being exceptional flood years.

These correlations are important as they allow stakeholders to estimate the flooded areas based on observed, accessible hydrological data. These regression models notably update the previous equations developed using seven SPOT images from the 1990s (Lamagat and Bader, 2004), improving the assessment of flooded areas by leveraging advances in earth observations. Updating these regressions has also ensured that they reflect the changes in hydrological regime observed over the past decades. These models have direct operational consequences as they are used to predict the amplitude of the flooded area and guide reservoir operation to support FBAS activities in the floodplain. The river basin agency (OMVS) currently exploits such correlations to define reservoir operation rules in order to maintain at least 50,000 ha of FBAS and to design the Senegal river basin development master plan (SCP et al., 2009; Bader, 2015; BRLi et al., 2021). Results also point to the increase in reliability when estimating peak flooded areas based on upstream flows in August–September vs. August alone which leads to much larger uncertainties. Future research on hydrodynamic modelling based on high resolution digital elevation models should help refine estimates of flooded areas, notably for high stage values outside the range observed over 2000–2022.

4.3. Mapping FBAS potential areas and modelling long term trends in cultivated areas

FBAS remain poorly documented, despite the millions of hectares in Africa and Asia which support the livelihoods of millions of smallholder farmers (Kool et al., 2018). Unlike irrigated systems that have been widely investigated with earth observations, there are very few studies which focus specifically on mapping FBAS practices using EO (Mané and Fraval, 2001; Poussin et al., 2020). The heterogeneous, small scale cropping activities are difficult to distinguish especially when working at large scales and over extended periods. Studies on FBAS focus predominantly on characterising and improving the productivity of these practices (Kool et al., 2018; Ayyad et al., 2022; Sall et al., 2020b,a; Zenebe et al., 2022). Here, we developed an approach to map FBAS potential areas and estimate FBAS cropped areas based on the knowledge of surface water dynamics in the floodplain. Characterising inundation dynamics in floodplains is an essential step to understand FBAS practices and potential FBAS areas. In East Africa, Harou et al. (2020) similarly exploited MODIS data and Bayesian networks to predict plausible areas for FBAS.

Correlations between flooded areas and available statistics on FBAS enabled the estimation of total FBAS cultivated areas in the floodplain and their variations over the past 72 years. Results show that values of 100,000 ha of cropped FBAS were regularly exceeded between 1950 and 1971. This is in agreement with Dieye et al. (2020) who estimated 108,000 ha cultivated over 1946–1971. Similarly, Dickmann et al. (2009) estimated that 114,000 ha were cultivated (out of a FBAS potential of 233,000 ha) before 1971 and the onset of droughts across the Sahel. Since 1994 and the return of greater flooded areas, the average FBAS cropped area is estimated here around 57,000 ha, but with high inter-annual variations. The current scale of FBAS practices remains hard to confirm but partial statistics by the Senegal government provides an estimate of surface areas per crop (DAPSA, 2021). Considering only the departments bordering the river (Dagana, Podor, Matam, Kanel and Bakel) the total area cropped for key recession crops (sorghum, millet and cowpea) reach 54,000 ha during the large 2022 flood. Previous analysis of data in Lamagat (2001) led to an estimate of a 66–34 ratio between cropped areas on the Senegalese and Mauritanian sides, which would lead to an estimate of 36,000 on the right bank and a total of 90,000 ha. Despite uncertainties as to the part actually cultivated on the Senegal floodplain per department and double cropping of cowpea–sorghum, the result is remarkably comparable to the 87,000 ha estimated for 2022 from our regression model. At the same time, our S2 water occurrence maps identified 188,000 ha as potentially suitable land for FBAS in 2022. Literature suggests that in the floodplain around 50% of land suitable for FBAS is effectively cropped (Mané and Fraval, 2001; Dickmann et al., 2009; Poussin et al., 2020). On this assumption, up to 94,000 ha may have been cropped in 2022, further supporting the consistency of estimates derived from both water occurrence maps and regression models.

In parallel, this research led to the first assessment for the Senegal river floodplain of the areas suitable for FBAS. Annual and multi-year water occurrence maps produced from Sentinel-2 observations are valuable results to visualise the dynamics of the flood, identify dryland, permanent flooded areas and temporary flooded areas which may be relevant for recession farming. These improve upon available Global Surface Water occurrence maps (Pekel et al., 2016) due to the greater detection of heterogeneous flooded areas achieved here. The thresholds applied in this approach seek to remove uncertainties from clouds, occasional rainfall events and wet season irrigation but some of these may lead to pixels being wrongly classified as temporarily flooded. Experience working in the region with local farmers shows that excluding these pixels is complex as certain parts of irrigated perimeters may well become flooded during large flood events, as seen in the top left of Fig. 11. The maps combine imagery between September and November, therefore excluding dry season irrigated perimeters. Flood occurrence maps provide spatialised information to enable farmers and stakeholders to better appreciate areas which are flooded most often and help determine suitable plots. These results are important for stakeholders to appreciate the potential of FBAS in the floodplain. These maps also have other applications in hydrology notably to improve research on evaporation over flooded areas, the water balance (Kool et al., 2022) and to support the calibration of 2D hydrodynamic models of floodplains (Jafarzadegan et al., 2023).

The estimates of areas suitable for FBAS and of total FBAS cultivated areas were based on hydrological variables. Sufficient water reserves in the soil are the most limiting factor (Sall et al., 2020b). Bader et al. (2003) previously estimated that FBAS suitable areas required a minimum flood duration of 25 days. Analysis of the S2 occurrence maps over 446 FBAS plots in Podor, Senegal showed here that areas effectively used for FBAS were flooded between 19 and 57 days. Farmers indicate that a flood duration of 15 to 60 days is required to allow recession cropping (Sall et al., 2020a), highlighting a strong coherence between our results and the farmers' observations and knowledge. In areas where water stagnates for too long, land is not cultivated. This can be due to dense natural vegetation that thrives as a result of being regularly flooded, but also for reasons related to the agricultural calendar. Farmers typically sow sorghum and cowpea crops in October-November as the flood recedes. Flood waters however need to retreat sufficiently early to allow sorghum crops to be sown and grow before the temperatures drop (Poussin et al., 2020). Cropping plots in December leads to reduced yields as sorghum is a photoperiodic crop (Chantereau et al., 2013). In addition, farmers need to have harvested FBAS crops in time to start working on the dry season irrigated crops (onions, rice). By considering areas flooded up to 57 days, this approach ensured that most years the flood will have receded by the end of November. Depending on the amplitude of the annual flood, this corresponds to a total area ranging between 50,000 ha and 200,000 ha which has the potential to support FBAS. FBAS, like other agricultural practices, are driven by several factors. Water availability is not the only driver (Ogilvie et al., 2019) and FBAS will depend on numerous factors including proximity for farmers, land tenure and socio-economic difficulties which must be investigated locally (Sall et al., 2020a). These results underline the need for local assessments of FBAS practices, and argue for better collection of national statistics on flood-based agriculture (Sidibe et al., 2016; Poussin et al., 2020). Further research exploiting remote sensing and in situ observations to map the actual cropped areas will also help confirm how FBAS practices have evolved following hydro-climatic changes and socio-economic shifts in the region.

5. Conclusions

By combining earth observations, hydrological regression models and extensive fieldwork, this research provides a detailed understanding of water surface dynamics and flood-based agricultural systems in the Senegal river floodplain. These works demonstrate the effectiveness of optical EO data in capturing long-term interannual variations across a large semi-arid floodplain and producing the most comprehensive maps of temporary inundated areas. Regressive models, trained with hydrological data and agricultural field observations, enable the analysis of long term trends in flooded and FBAS cropped areas from 1950 to 2022. These findings reveal the return of strong floods since the mid-1990s, as well as the pronounced variability experienced by FBAS farmers due to climatic and human-induced changes, including the operation of the Manantali dam. Predictive models for annual flooded and cropped areas based on upstream flows can guide early warning systems for farmers, authorities, and aid agencies, granting better preparation for extreme floods and droughts. However, growing water demands for hydropower and irrigation during the dry season are at odds with these livelihoods strategies, which rely on annual floods. Predictive models developed here will help quantify the impacts of future dams on peak flows and FBAS, allowing for the definition of optimal water allocation strategies that balance the competing needs of the water-energy-food-ecosystems nexus.

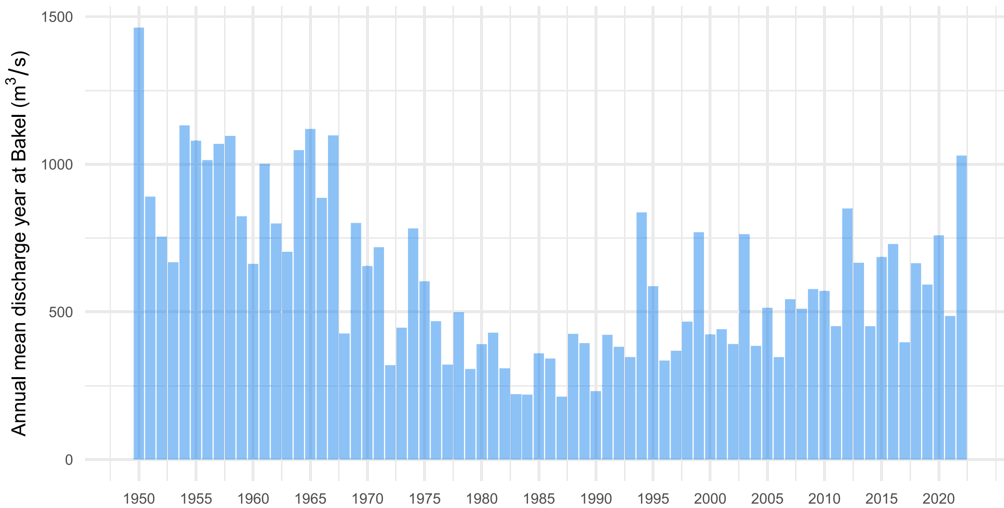

Fig. A.1. Mean annual flow at Bakel over 1950–2022. Flow is calculated over the hydrological year, e.g. for 2022 using flow data from June 2022 to May 2023.

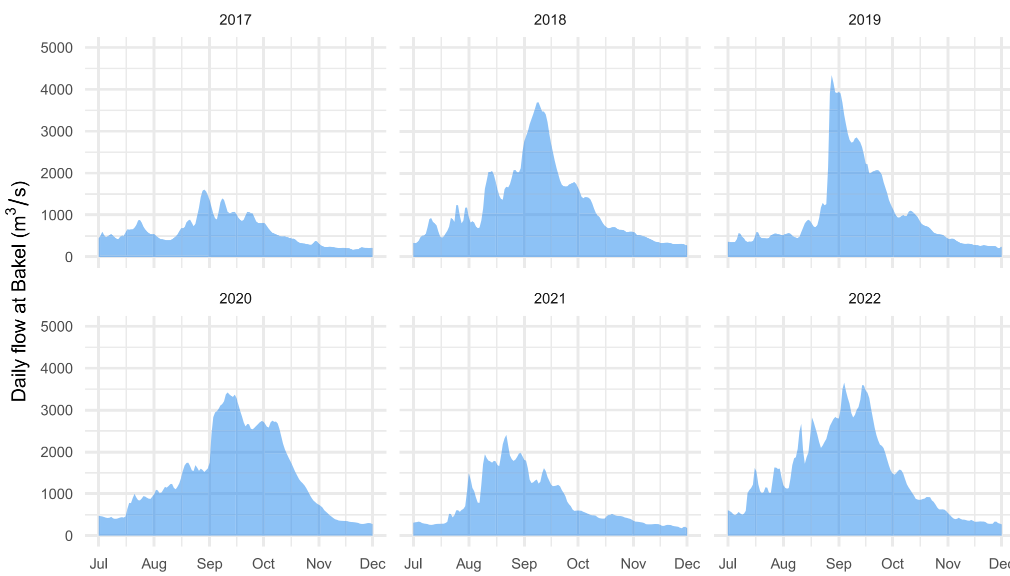

Fig. A.2. Flow hydrographs at Bakel gauging station for 2017–2022.

CRediT authorship contribution statement

Andrew Ogilvie: Writing – review & editing, Writing – original draft, Project administration, Methodology, Investigation, Funding acquisition, Formal analysis, Data curation, Conceptualization. **Cheickh Sadibou Fall:** Writing – review & editing, Investigation. **Ansoumana Bodian:** Writing – review & editing, Funding acquisition. **Didier Martin:** Resources, Investigation, Data curation. **Laurent Bruckmann:** Writing – review & editing, Validation. **Djiby Dia:** Writing – review & editing, Supervision, Project administration. **Issa Leye:** Data curation. **Papa Malick Ndiaye:** Data curation. **Donissongou Dimitri Soro:** Funding acquisition, Data curation. **Jean Homian Danumah:** Funding acquisition, Writing – review & editing. **Jean-Claude Bader:** Methodology, Data curation, Conceptualization. **Jean-Christophe Poussin:** Writing – review & editing, Supervision, Project administration, Funding acquisition.

Declaration of competing interest

The authors declare that they have no known competing financial interests or personal relationships that could have appeared to influence the work reported in this paper.

Acknowledgements

This research was supported by the AFD CECC (Cycle de l'Eau et Changement Climatique) project, the ESA EO-for-Africa RFCMACC project, the ANR LEAP-AGRI WAGRINNOVA project (grant number ANR-18-LEAP-0002), EU-funded AICS N.03/2020 WEFE-SENEGAL project and the One Planet Fellowship Programme (GA 406 569/LabEx AGRO 2011-LABX-002).

We gratefully acknowledge the Direction Nationale de l'Hydraulique of Senegal for the hydrological data, USGS and ESA for the earth observations and Google Earth Engine for the cloud computing. Finally, we thank the academic editor, the guest editor and three anonymous reviewers for their comments that helped strengthen the manuscript.

Appendix

See Figs. A.1–A.5.

Data availability

Data will be made available on request.

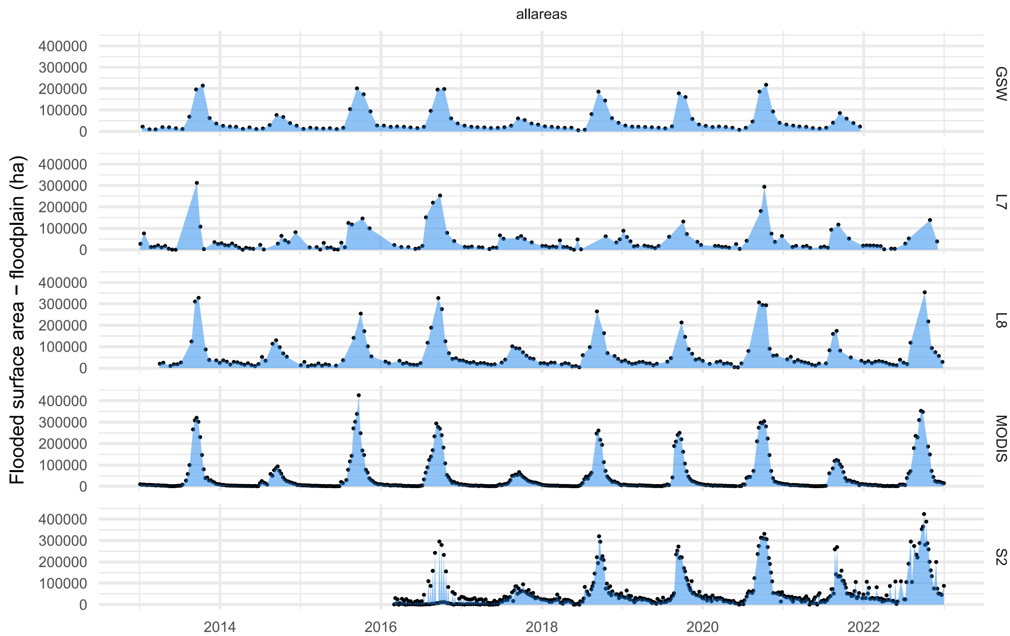

Fig. A.3. Flooded surface area in Senegal river floodplain over the past ten years (2013–2022) based on 5 satellite sources.

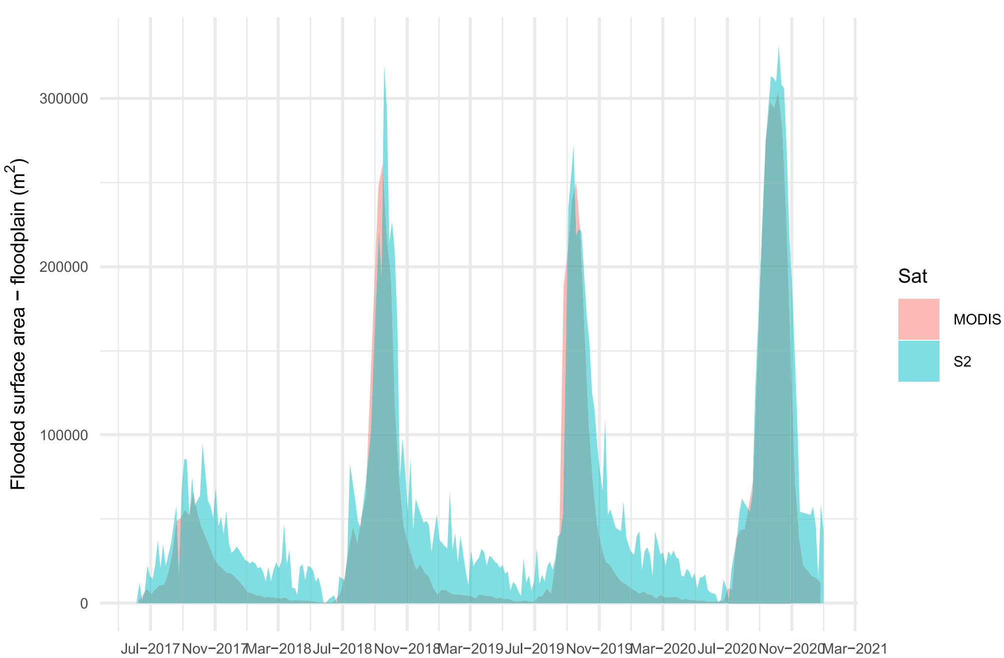

Fig. A.4. Comparison between MODIS and Sentinel-2 estimates of flood dynamics of Senegal floodplain (2017–2020).

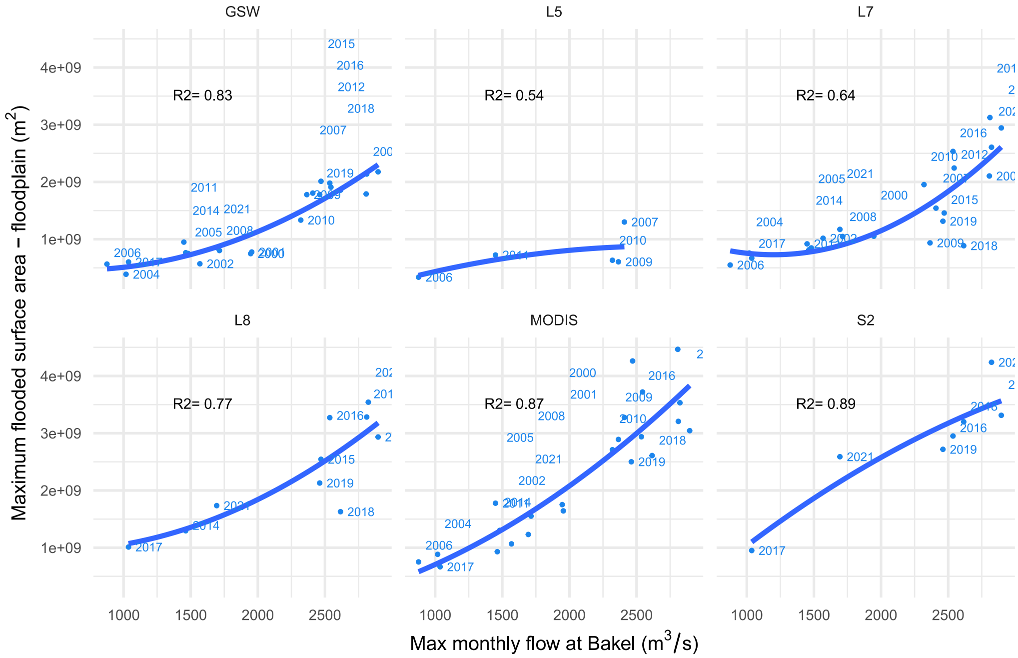

Fig. A.5. Relationships between peak monthly flow data at Bakel and peak water surface area detected by each EO source per year over 2000–2022.

References

Aires, F., Prigent, C., Fluet-Chouinard, E., Yamazaki, D., Papa, F., Lehner, B., 2018. Comparison of visible and multi-satellite global inundation datasets at high-spatial resolution. Remote Sens. Environ. 216, http://dx.doi.org/10.1016/j.rse.2018.06.015.

Aires, F., Venot, J.P., Massuel, S., Gratiot, N., Pham-Duc, B., Prigent, C., 2020. Surface water evolution (2001–2017) at the cambodia/vietnam border in the upper mekong delta using satellite modis observations. Remote Sens. 12, http://dx.doi.org/10.3390/rs12050800.

Amani, M., Brisco, B., Afshar, M., Mirmazloumi, S.M., Mahdavi, S., Mirzadeh, S.M.J., Huang, W., Granger, J., 2019. A generalized supervised classification scheme to produce provincial wetland inventory maps: an application of google earth engine for big geo data processing. Big Earth Data 3, 378–394. http://dx.doi.org/10.1080/20964471.2019.1690404.

ANSD, 2014. Recensement général de la population et de l'habitat, de l'agriculture et de l'elevage 2013.

Archer, L., Neal, J.C., Bates, P.D., House, J.I., 2018. Comparing tandem-x data with frequently-used dems for flood inundation modelling. Water Resour. Res. http://dx.doi.org/10.1029/2018WR023688.

Ayyad, S., Karimi, P., Langensiepen, M., Ribbe, L., Rebelo, L.M., Becker, M., 2022. Remote sensing assessment of available green water to increase crop production in seasonal floodplain wetlands of sub-saharan africa. Agricult. Water. Manag. 269, http://dx.doi.org/10.1016/j.agwat.2022.107712.

Bader, J.C., 1997. Le soutien de crue mobile dans le fleuve sénégal, à partir du barrage de manantali. Hydrol. Sci. J. 42, 815–831. http://dx.doi.org/10.1080/02626669709492081.

Bader, J.C., 2015. Monographie hydrologique du fleuve Sénégal: de l'origine des mesures jusqu'en 2011. Ird ed.

Bader, J.C., Belaud, G., Lamagat, J.P., Ferret, T., Vauchel, P., 2017. Modélisation de propagation d'écoulement entre lits mineur et majeur sur les fleuves sénégal et niger. Hydrol. Sci. J. 62, 447–466. http://dx.doi.org/10.1080/02626667.2016.1148815.

Bader, J.C., Lamagat, J.P., Guiguen, N., 2003. Management of the manantali dam on the senegal river: Quantitative analysis of a conflict of objectives. Hydrol. Sci. J. 48, 525–538. http://dx.doi.org/10.1623/hysj.48.4.525.51415.

Bergé-Nguyen, M., Crétaux, J.F., 2015. Inundations in the inner niger delta: Monitoring and analysis using modis and global precipitation datasets. Remote Sens. 7, 2127–2151. http://dx.doi.org/10.3390/rs70202127.

Bodian, A., Diop, L., Panthou, G., Dacosta, H., Deme, A., Dezetter, A., Ndiaye, P.M., Diouf, I., Vischel, T., 2020. Recent trend in hydroclimatic conditions in the senegal river basin. Water 12 (436), http://dx.doi.org/10.3390/w12020436.

BRLi, CSE, IRD, 2021. Révision du schéma directeur d'aménagement et de gestion des eaux (sdage) du fleuve sénégal à l'horizon 2050. etat des lieux et diagnostics sectoriels, https://cda-omvs.org/14995-revision-du-schema-directeur-damenagement-et-de-gestion-des-eaux-sdage-du-fleuve-senegal-a-lhorizon-2050-evaluation-diagnostics-sectoriels-et-enjeux-etat-des-lieux-et-diagnostics-sect/.

Bruckmann, L., 2018. Crue et développement rural dans la vallée du sénégal : entre marginalisation et résilience. BELGEO http://dx.doi.org/10.4000/belgeo.23158.

Bruckmann, L., Delbart, N., Descroix, L., Bodian, A., 2022. Recent hydrological evolutions of the senegal river flood (West Africa). Hydrol. Sci. J. 67, 385–400. http://dx.doi.org/10.1080/02626667.2021.1998511.

Chantereau, J., Cruz, J.F., Ratnadass, A., Trouche, G., Fliedel, G., 2013. Le sorgho. http://dx.doi.org/10.35690/978-2-7592-2062-5.

Claverie, M., Ju, J., Masek, J.G., Dungan, J.L., Vermote, E.F., Roger, J.C., Skakun, S.V., Justice, C., 2018. The harmonized landsat and sentinel-2 surface reflectance data set. Remote Sens. Environ. 219, 145–161. http://dx.doi.org/10.1016/J.RSE.2018.09.002.

Cristiano, E., Deidda, R., Viola, F., 2021. The role of green roofs in urban water-energy-food-ecosystem nexus: A review. Sci. Total Environ. 756, http://dx.doi.org/10.1016/j.scitotenv.2020.143876.

Dakhlaoui, H., Ruelland, D., Tramblay, Y., 2019. A bootstrap-based differential split-sample test to assess the transferability of conceptual rainfall-runoff models under past and future climate variability. J. Hydrol. 575, http://dx.doi.org/10.1016/j.jhydrol.2019.05.056.

d'Andrimont, R., Defourny, P., 2018. Monitoring African water bodies from twice-daily modis observation. GISci. Remote Sens. 55, 130–153. http://dx.doi.org/10.1080/15481603.2017.1366677.

DAPSA, 2021. Rapport de l'enquête agricole annuelle (eaa) 2020-2021. https://www.dapsa.gouv.sn/sites/default/files/publications/Rapport%20EAA%202020-2021_finale.pdf.

Descroix, L., Faty, B., Manga, S.P., Diedhiou, A.B., Lambert, L.A., Soumaré, S., Andrieu, J., Ogilvie, A., Fall, A., Mahé, G., Diallo, F.B.S., Diallo, A., Diallo, K., Albergel, J., Tanimoun, B.A., Amadou, I., Bader, J.C., Barry, A., Bodian, A., Boulvert, Y., Braquet, N., Couture, J.L., Dacosta, H., Dejacquelot, G., Diakité, M., Diallo, K., Gallese, E., Ferry, L., Konaté, L., Nnomo, B.N., Olivry, J.C., Orange, D., Sakho, Y., Sambou, S., Vandervaere, J.P., 2020. Are the fouta djallon highlands still the water tower of West Africa? Water (Switzerland) 12, http://dx.doi.org/10.3390/w12112968.

Dickmann, M., Sieburger, D., Ficatier, M., Naudet, M., Schmidt, M., Seve, M., 2009. The manantali dam. synthesis report.

Dieye, M., Dia, D., Barbier, B., Sylla, E., Sall, M., Bader, J.C., Bossa, A., Sanfo, S., Fall, C., 2020. Chapitre 8. L'agriculture de décrue en Afrique de l'Ouest et du centre, IRD Editions pp. 121–131. http://dx.doi.org/10.4000/books.irdeditions.36264.

Donchyts, G., Baart, F., Winsemius, H., Gorelick, N., Kwadijk, J., van de Giesen, N., 2016. Earth's surface water change over the past 30 years. Nature Clim. Change 6, 810–813. http://dx.doi.org/10.1038/nclimate3111.

Feng, Q., Liu, J., Gong, J., 2015. Uav remote sensing for urban vegetation mapping using random forest and texture analysis. Remote Sens. 7, 1074–1094. http://dx.doi.org/10.3390/rs70101074.

Gao, F., Masek, J., Schwaller, M., Hall, F., 2006. On the blending of the landsat and modis surface reflectance: predicting daily landsat surface reflectance. IEEE Trans. Geosci. Remote Sens. 44, 2207–2218. http://dx.doi.org/10.1109/TGRS.2006.872081.

Gorelick, N., Hancher, M., Dixon, M., Ilyushchenko, S., Thau, D., Moore, R., 2017. Google earth engine: Planetary-scale geospatial analysis for everyone. Remote Sens. Environ. 202, 18–27. http://dx.doi.org/10.1016/J.RSE.2017.06.031.

Hannah, D.M., Demuth, S., van Lanen, H.A., Looser, U., Prudhomme, C., Rees, G., Stahl, K., Tallaksen, L.M., 2011. Large-scale river flow archives: Importance, current status and future needs. Hydrol. Process. 25, http://dx.doi.org/10.1002/hyp.7794.

Hardy, A., Ettritch, G., Cross, D.E., Bunting, P., Liywalii, F., Sakala, J., Silumesii, A., Singini, D., Smith, M., Willis, T., Thomas, C.J., 2019. Automatic detection of open and vegetated water bodies using sentinel 1 to map African malaria vector mosquito breeding habitats. Remote Sens. 11, http://dx.doi.org/10.3390/rs11050593.

Harou, I.L., Whitney, C., Kung'u, J., Luedeling, E., 2020. Mapping flood-based farming systems with bayesian networks. Land 9 (369), http://dx.doi.org/10.3390/land9100369.

Hawker, L., Bates, P., Neal, J., Rougier, J., 2018. Perspectives on digital elevation model (dem) simulation for flood modeling in the absence of a high-accuracy open access global dem. Front. Earth Sci. 6 (233), http://dx.doi.org/10.3389/feart.2018.00233.

Hecht, J.S., Lacombe, G., Arias, M.E., Dang, T.D., Piman, T., 2019. Hydropower dams of the mekong river basin: A review of their hydrological impacts. J. Hydrol. 568, 285–300. http://dx.doi.org/10.1016/j.jhydrol.2018.10.045.

Heimhuber, V., Tulbure, M.G., Broich, M., 2018. Addressing spatio-temporal resolution constraints in landsat and modis-based mapping of large-scale floodplain inundation dynamics. Remote Sens. Environ. 211, 307–320. http://dx.doi.org/10.1016/j.rse.2018.04.016.

Hellegers, P., Zilberman, D., Steduto, P., McCornick, P., 2008. Interactions between water, energy, food and environment: evolving perspectives and policy issues. Water Policy 10, http://dx.doi.org/10.2166/wp.2008.048.

Herndon, K., Muench, R., Cherrington, E., Griffin, R., 2020. An assessment of surface water detection methods for water resource management in the nigerien sahel. Sensors 20 (431), http://dx.doi.org/10.3390/s20020431.

Htitiou, A., Boudhar, A., Benabdelouahab, T., 2021. Deep learning-based spatiotemporal fusion approach for producing high-resolution ndvi time-series datasets. Can. J. Remote Sens. 47, http://dx.doi.org/10.1080/07038992.2020.1865141.

Huang, C., 2018. Seeing surface water from space. Eos 99, http://dx.doi.org/10.1029/2018EO103123.

Jafarzadegan, K., Moradkhani, H., Pappenberger, F., Moftakhari, H., Bates, P., Abbaszadeh, P., Marsooli, R., Ferreira, C., Cloke, H.L., Ogden, F., Duan, Q., 2023. Recent advances and new frontiers in riverine and coastal flood modeling. Rev. Geophys. 61, http://dx.doi.org/10.1029/2022rg000788.

Ji, L., Zhang, L., Wylie, B., 2009. Analysis of dynamic thresholds for the normalized difference water index. Photogramm. Eng. Remote Sens. 75, 1307–1317. http://dx.doi.org/10.14358/PERS.75.11.1307.

Jung, H.C., Alsdorf, D., Moritz, M., Lee, H., Vassolo, S., 2011. Analysis of the relationship between flooding area and water height in the logone floodplain. Phys. Chem. Earth 36, 232–240. http://dx.doi.org/10.1016/j.pce.2011.01.010.

Kool, J., Lhermitte, S., Hrachowitz, M., Bregoli, F., McClain, M.E., 2022. Seasonal inundation dynamics and water balance of the mara wetland, tanzania based on multi-temporal sentinel-2 image classification. Int. J. Appl. Earth Obs. Geoinf. 109, http://dx.doi.org/10.1016/j.jag.2022.102766.

Kool, M., van Steenbergen, F., Haile, A.M., Abbas, Y.M., Hagos, E., 2018. The Promise of Flood-Based Farming Systems in Arid and Semi-arid Areas. Springer, Cham, pp. 77–94. http://dx.doi.org/10.1007/978-3-319-66239-8_5.

Lamagat, J.P., 2001. Programme d'optimisation de la gestion des réservoirs : phase 3 : crue artificielle et cultures de décrue : synthèse finale. pp. 1–67, https://www.documentation.ird.fr/hor/fdi:010051101.

Lamagat, J.P., Bader, J.C., 2004. Gestion intégrée des ressources en eau du bassin du Sénégal : programme d'optimisation de la gestion des réservoirs. CIRAD, p. 14, https://www.documentation.ird.fr/hor/fdi:0100076772.

Lehner, B., Liermann, C.R., Revenga, C., Vörösmarty, C., Fekete, B., Crouzet, P., Döll, P., Endejan, M., Frenken, K., Magome, J., Nilsson, C., Robertson, J.C., Rödel, R., Sindorf, N., Wisser, D., 2011. High-resolution mapping of the world's reservoirs and dams for sustainable river-flow management. Front. Ecol. Environ. 9, 494–502. http://dx.doi.org/10.1890/100125.

Li, W., Du, Z., Ling, F., Zhou, D., Wang, H., Gui, Y., Sun, B., Zhang, X., 2013. A comparison of land surface water mapping using the normalized difference water index from tm, etm+ and ali. Remote Sens. 5, 5530–5549. http://dx.doi.org/10.3390/rs5115530.

Li, L., Vrieling, A., Skidmore, A., Wang, T., Turak, E., 2018. Monitoring the dynamics of surface water fraction from modis time series in a mediterranean environment. Int. J. Appl. Earth Obs. Geoinf. 66, http://dx.doi.org/10.1016/j.jag.2017.11.007.

Liu, D., 2020. A rational performance criterion for hydrological model. J. Hydrol. 590, http://dx.doi.org/10.1016/j.jhydrol.2020.125488.

Mahdavi, S., Salehi, B., Granger, J., Amani, M., Brisco, B., Huang, W., 2018. Remote sensing for wetland classification: a comprehensive review. GISci. Remote Sens. 55, 623–658. http://dx.doi.org/10.1080/15481603.2017.1419602.

Mahdianpari, M., Salehi, B., Mohammadimanesh, F., Homayouni, S., Gill, E., 2018. The first wetland inventory map of newfoundland at a spatial resolution of 10 m using sentinel-1 and sentinel-2 data on the google earth engine cloud computing platform. Remote Sens. 11 (43), http://dx.doi.org/10.3390/rs11010043.

Mané, L., Fraval, P., 2001. Suivi par télédétection des cultures de décrue dans la vallée du fleuve sénégal en saison froide 2000/2001.

Mettrop, I., Wymenga, E., Klop, E., Bekkema, M., 2019. Impacts du changement climatique dans le bassin du fleuve sénégal: une évaluation spatiale de la vulnérabilité - a & w rapport. p. 2253.

Motavita, D.F., Chow, R., Guthke, A., Nowak, W., 2019. The comprehensive differential split-sample test: A stress-test for hydrological model robustness under climate variability. J. Hydrol. 573, http://dx.doi.org/10.1016/j.jhydrol.2019.03.054.

Nguyen, M.D., Baez-Villanueva, O.M., Bui, D.D., Nguyen, P.T., Ribbe, L., 2020. Harmonization of landsat and sentinel 2 for crop monitoring in drought prone areas: Case studies of ninh thuan (vietnam) and bekaa (lebanon). Remote Sens. 12 (281), http://dx.doi.org/10.3390/rs12020281.

Ogilvie, A., Belaud, G., Delenne, C., Bailly, J.S., Bader, J.C., Oleksiak, A., Ferry, L., Martin, D., 2015. Decadal monitoring of the niger inner delta flood dynamics using modis optical data. J. Hydrol. 523, 368–383. http://dx.doi.org/10.1016/j.jhydrol.2015.01.036.

Ogilvie, A., Belaud, G., Massuel, S., Mulligan, M., Goulven, P.L., Calvez, R., 2018. Surface water monitoring in small water bodies: potential and limits of multi-sensor landsat time series. Hydrol. Earth Syst. Sci. http://dx.doi.org/10.5194/hess-22-4349-2018.

Ogilvie, A., Poussin, J.C., Bader, J.C., Bayo, F., Bodian, A., Dacosta, H., Dia, D., Diop, L., Martin, D., Sambou, S., 2020a. Combining multi-sensor satellite imagery to improve long-term monitoring of temporary surface water bodies in the senegal river floodplain. Remote Sens. 12 (3157), http://dx.doi.org/10.3390/rs12193157.

Ogilvie, A., Poussin, J.C., Bader, J.C., Martin, D., Ndiaye, G., DIa, D., 2020b. Improved understanding of the senegal floodplain socio-hydrosystems with multi-scalar earth observations. In: Proceedings of the International Association of Hydrological Sciences. http://dx.doi.org/10.5194/piahs-383-255-2020.

Ogilvie, A., Riaux, J., Massuel, S., Mulligan, M., Belaud, G., Goulven, P.L., Calvez, R., 2019. Socio-hydrological drivers of agricultural water use in small reservoirs. Agricult. Water. Manag. http://dx.doi.org/10.1016/j.agwat.2019.03.001.

Orieschnig, C., Venot, J.P., Massuel, S., Eang, K.E., Chhuon, K., Lun, S., Siev, S., Belaud, G., 2022. A multi-method approach to flood mapping: Reconstructing inundation changes in the cambodian upper mekong delta. J. Hydrol. 610, 127902. http://dx.doi.org/10.1016/J.JHYDROL.2022.127902.

Padi, P.T., Baldassarre, G.D., Castellarin, A., 2011. Floodplain management in africa: Large scale analysis of flood data. Phys. Chem. Earth 36, 292–298. http://dx.doi.org/10.1016/j.pce.2011.02.002.

Papy, L., 1951. La vallée du sénégal: Agriculture traditionnelle et riziculture mécanisée. Cahiers d'Outre-Mer 4, 277–324.

Pekel, J.F., Cottam, A., Gorelick, N., Belward, A.S., 2016. High-resolution mapping of global surface water and its long-term changes. Nature 540, 418–422. http://dx.doi.org/10.1038/nature20584.

Poussin, J.C., Martin, D., Bader, J.C., Dia, D., Seck, S.M., Ogilvie, A., 2020. Variabilité agro-hydrologique des cultures de décrue. une étude de cas dans la moyenne vallée du fleuve sénégal. Cahiers Agric. 29, 23. http://dx.doi.org/10.1051/cagri/2020022.

Raso, L., Bader, J.C., Weijs, S., 2020. Reservoir operation optimized for hydropower production reduces conflict with traditional water uses in the senegal river. J. Water Resour. Plan. Manag. 146, 05020003. http://dx.doi.org/10.1061/(ASCE)WR.1943-5452.0001076.

Sall, M., Ndiaye, R., Cissé, M., Sine, B., Ndiaye, M., Ndongo, H., 2020a. Chapitre 12. Amélioration des pratiques culturales du sorgho de décrue dans la moyenne vallée du fleuve Sénégal, IRD Editions pp. 163–178. http://dx.doi.org/10.4000/books.irdeditions.36329, http://books.openedition.org/irdeditions/36329.

Sall, M., Poussin, J.C., Bossa, A.Y., Ndiaye, R., Cissé, M., Martin, D., Bader, J.C., Sultan, B., Ogilvie, A., 2020b. Water constraints and flood-recession agriculture in the senegal river valley. Atmosphere 11, http://dx.doi.org/10.3390/atmos11111192.

Sambou, S., Diémé, Y., Touré, A.K., Badji, A.M., Malanda-Nimy, E.N., 2019. Effet du barrage de manantali sur les modifications du régime hydrologique du fleuve sénégal dans le bassin amont : une approche statistique. Sécheresse 20, 104–111. http://dx.doi.org/10.1684/sec.2009.0176.

SCP, CSE, CACG, Ginger, 2009. Sdage du fleuve sénégal. phase 1. état des lieux et diagnostic.

Seidou, O., Ringler, C., Kalcic, S., Ferrini, L., Ramani, T.A., Guero, A., 2021. A semi-qualitative approach to the operationalization of the food–environment–energy–water (fe2w) nexus concept for infrastructure planning: a case study of the niger basin. Water Int. 46, 744–770. http://dx.doi.org/10.1080/02508060.2021.1956231.

Sidibe, Y., Williams, T.O., Kolavalli, S., 2016. Flood recession agriculture for food security in northern ghana: literature review on extent, challenges, and opportunities. http://dx.doi.org/10.13140/RG.2.1.3250.8405.

Stehman, S.V., Foody, G.M., 2019. Key issues in rigorous accuracy assessment of land cover products. Remote Sens. Environ. 231, 111199. http://dx.doi.org/10.1016/j.rse.2019.05.018.

Tarpanelli, A., Paris, A., Sichangi, A.W., O'Loughlin, F., Papa, F., 2023. Water resources in africa: The role of earth observation data and hydrodynamic modeling to derive river discharge. Surv. Geophys. 44, http://dx.doi.org/10.1007/s10712-022-09744-x.

Teutschbein, C., Jonsson, E., Todorović, A., Tootoonchi, F., Stenfors, E., Grabs, T., 2023. Future drought propagation through the water-energy-food-ecosystem nexus – a nordic perspective. J. Hydrol. 617, http://dx.doi.org/10.1016/j.jhydrol.2022.128963.

Tilmant, A., Pina, J., Salman, M., Casarotto, C., Ledbi, F., Pek, E., 2020. Probabilistic trade-off assessment between competing and vulnerable water users – the case of the senegal river basin. J. Hydrol. 587, 124915. http://dx.doi.org/10.1016/j.jhydrol.2020.124915.

Verdin, K., 2017. Hydrologic derivatives for modeling and analysis—a new global high-resolution database. http://dx.doi.org/10.3133/ds1053, data series 1053.

Xiao, J., Aggarwal, A.K., Duc, N.H., Arya, A., Rage, U.K., Avtar, R., 2023. A review of remote sensing image spatiotemporal fusion: challenges, applications and recent trends. http://dx.doi.org/10.1016/j.rsase.2023.101005.

Xiao, D., Niu, H., Guo, F., Zhao, S., Fan, L., 2022. Monitoring irrigation dynamics in paddy fields using spatiotemporal fusion of sentinel-2 and modis. Agricult. Water. Manag. 263, http://dx.doi.org/10.1016/j.agwat.2021.107409.

Xu, H., 2006. Modification of normalised difference water index (ndwi) to enhance open water features in remotely sensed imagery. Int. J. Remote Sens. 27, 3025–3033. http://dx.doi.org/10.1080/01431160600589179.

Yamazaki, D., Trigg, M.A., 2016. Hydrology: The dynamics of earth's surface water. Nature 540, 348–349. http://dx.doi.org/10.1038/nature21100.

Yamazaki, D., Trigg, M.A., Ikeshima, D., 2015. Development of a global 90 m water body map using multi-temporal landsat images. Remote Sens. Environ. 171, 337–351. http://dx.doi.org/10.1016/j.rse.2015.10.014.

Yang, X., Qin, Q., Yésou, H., Ledauphin, T., Koehl, M., Grussenmeyer, P., Zhu, Z., 2020. Monthly estimation of the surface water extent in france at a 10-m resolution using sentinel-2 data. Remote Sens. Environ. 244, http://dx.doi.org/10.1016/j.rse.2020.111803.

Zenebe, M.G., Fleskens, L., Ritsema, C., Steenbergen, F., 2022. Basin-wide productivity and livelihood analysis of flood-based agricultural systems in African drylands: A case study in the fogera floodplain. Agricult. Water. Manag. 261, http://dx.doi.org/10.1016/j.agwat.2021.107379.

Zhu, X., Chen, J., Gao, F., Chen, X., Masek, J.G., 2010. An enhanced spatial and temporal adaptive reflectance fusion model for complex heterogeneous regions. Remote Sens. Environ. 114, http://dx.doi.org/10.1016/j.rse.2010.05.032.